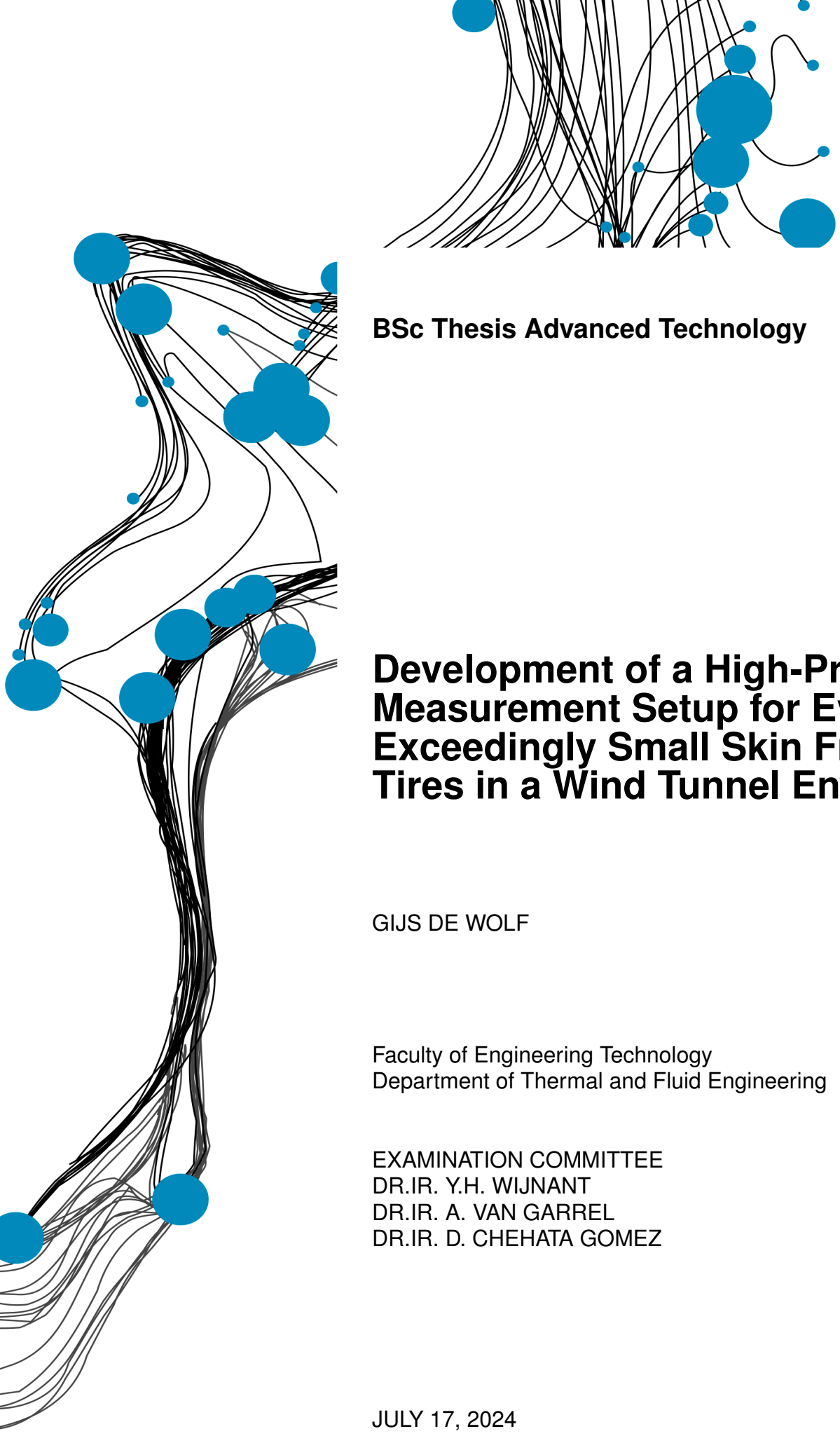

BSc Thesis Advanced Technology

Development of a High-Precision Measurement Setup for Evaluating Exceedingly Small Skin Friction Drag of Tires in a Wind Tunnel Environment

GIJS DE WOLF

Faculty of Engineering Technology
Department of Thermal and Fluid Engineering

EXAMINATION COMMITTEE
DR.IR. Y.H. WIJNANT
DR.IR. A. VAN GARREL
DR.IR. D. CHEHATA GOMEZ

JULY 17, 2024

Thesis submitted by
Gijs de Wolf
under the supervision of
dr.ir. Y.H. Wijnant
in order to fulfill the necessary requirements to obtain a Bachelor's degree in Advanced Technology at the
University of Twente
and defended on
Wednesday, 17th of July, 2024

Abstract

This study investigates the influence of various tire sidewall textures and the addition of a flash around the tire on the measured drag coefficient using a mass-spring system in a controlled wind tunnel environment. The primary objective is to isolate and quantify the skin friction drag induced by different tire textures or the addition of a flash, eliminating the effects of pressure drag and other external factors. A one-degree-of-freedom (1-DOF) mass-spring system with leaf springs was employed to ensure unidirectional movement and accurate force measurements. The setup included a stable, low-weight moving table made from Blocan pieces to support different tire sizes, ranging from small to large, each tested at six predefined airspeeds (0km/h, 42km/h, 64km/h, 86km/h, 109km/h, and 130km/h). Calibration of the system was achieved using a load cells and a Multi-Channel Amplifier, ensuring high sensitivity and precision in low-force ranges. Data analysis, performed using Matlab, involved normalizing the measurements to ensure consistent starting points across all plots. The results highlighted the effects of tire texture and design on drag force, demonstrating the importance of precise measurement setups and material choices in aerodynamic testing. This research contributes to a deeper understanding of the aerodynamic properties of tire sidewalls, with implications for improving vehicle performance and fuel efficiency. The results show a clear relation between texture roughness and the skin friction drag coefficient.

Table of Contents

List of Figures

List of Tables

1 Introduction

Over the years, car manufacturers and their collaborators have been optimizing their vehicle parts to enhance vehicle performance and safety. Among these components, tires play a crucial role. Acting as an interface between the car and the road, they influence traction, determine fuel consumption, and compensate for any irregularities in the road [1][2]. Integral to tire performance is drag. The drag of tires has two main components. Pressure drag and skin friction drag [3].

Pressure drag, also known as form drag [3], occurs due to the pressure difference between the front and back sides of an object moving through a fluid, such as air [4]. In the context of tires, pressure drag occurs primarily due to the shape of the tire and its interaction with the airflow surrounding the tire.

As a tire moves forward, it pushes through the air, creating high- and low-pressure areas around its surface [5]. At the front of the tire, the airflow is compressed, leading to a high-pressure zone [4]. This high-pressure area forms a force that works against the forward motion of the tire. On the other side of the tire, at the back, the airflow expands and separates from the surface, which results in a low-pressure area [5][6]. This low-pressure area forms suction forces that also act against the tire's forward motion. The pressure difference between the front and back sides of the tire generates an overall drag force, which is known as pressure drag [3]. This drag force works against the vehicle's movement, adding to the overall resistance experienced by the tire.

Skin friction drag is the drag between any fluid and the surface of an object [3][6]. In the context of tires, friction drag will arise on the side of the tire as it moves through the surrounding air [5]. A few factors influence the magnitude of this drag, including the texture of the tire surface and the velocity of the car.

In real-time, when a tire rolls along the ground, it displaces the surrounding air. This movement creates a region of disturbed airflow, more formally known as the boundary layer (See Fig. 1.1) [7][8]. This boundary layer consists of different layers, with different properties. Closest to the tire surface is the viscous sublayer, where the airflow is influenced the most by the presence of the tire's surface texture [9][10]. As air moves away from the tire, it transitions to a turbulent boundary layer [11]. The interaction between the tire surface and the air molecules in this viscous layer causes frictional forces, also known as skin friction forces [3][12]. These frictional forces act tangentially to the surface of the tire. These forces are responsible for the skin friction drag acting on the tire. Rougher surfaces tend to create more turbulence in the boundary layer, thus increasing the skin friction forces [13]. The velocity of the car is responsible for the intensity of the skin friction drag. Higher velocities will lead to more airflow around the tire, thus an increased turbulence and a higher friction drag [6][14].

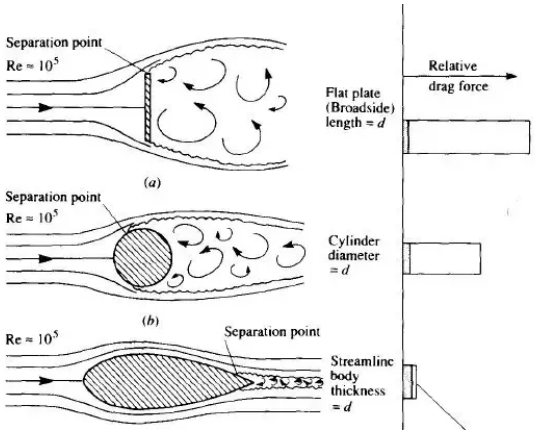

Figure 1.1: Boundary layers for different shaped objects placed in an air flow [15]

An interest for most tire producers is how to optimize a tire's drag performance. One of these tire companies is Apollo Tyres, a tire manufacturing company based in Enschede. The main focus of this research is to provide valuable insights to Apollo, regarding the influence of different "side-wall" (See Fig. 1.2) textures on their corresponding friction drag. Specifically, the study aims to show which textures exhibit the least amount of friction drag, thus offering Apollo valuable data for optimizing their tire designs. Additionally, the effects of the addition of a flash, which will be defined in Chapter 2.1, will be evaluated. The task at hand is to create a setup for the wind tunnel where the tires are positioned horizontally, and the skin friction drag is measured.

In this study, eight different tires are examined to show their impact on skin friction drag. The wind tunnel is used to precisely change and manipulate the velocity of airflow around the tire. The primary objective of these measurements is to analyze and compare the friction drag characteristics of distinct tire textures and designs, selected to represent a variety of surface designs and compositions. By conducting horizontal tests with the tires almost flush with the wind tunnel table, the study aims to focus on obtaining precise measurements of skin friction drag, on the side of the tires solely [16].

The friction drag caused by these tire textures is exceedingly small, which will be presented in Chapter 2.2, thus the measurement setup should be capable of measuring small variations. This means a highly sensitive and accurate setup is required.

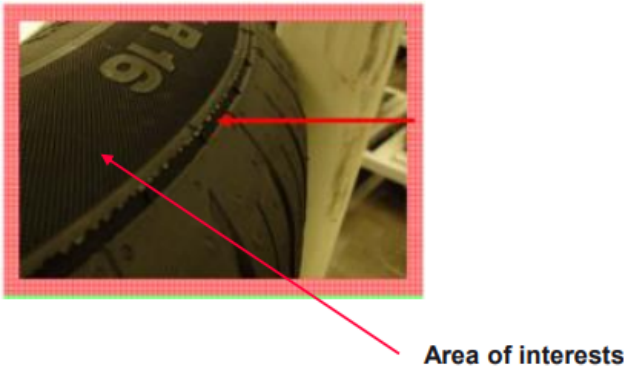

Figure 1.2: Area of interest to be inspected, determined by Apollo [17] *Note: The textured part of the tire will be referred to as sidewall from now on*

2 Background and Theory

2.1 Background

To get a better understanding of the differences in tires and the main focuses of this research, a little background information is given.

The main focus of this research is the development of a measurement setup within the wind tunnel facility of the University of Twente, and the measurement of skin friction drag. The wind tunnel's soundproofing and temperature control make it an excellent environment for studying the effects of different tire textures on skin friction drag without external influences. The wind tunnel is kept at roughly 22 degrees Celsius, to emulate average outside conditions.

Small	653.1mm
Medium	676.4mm
Large	695.9mm

Table 2.1: Diameters of the different tire sizes

In this wind tunnel, eight tires will be inspected. This includes two small tires, two medium tires, and four large tires. Their corresponding diameters are given in Tab. 2.1. One of the medium tires has a small strip of rubber, known as a 'flash'[1] [17] (See Fig. 2.1), which remains connected to the tire after production. Its effect on the airflow and drag coefficients will also be evaluated.

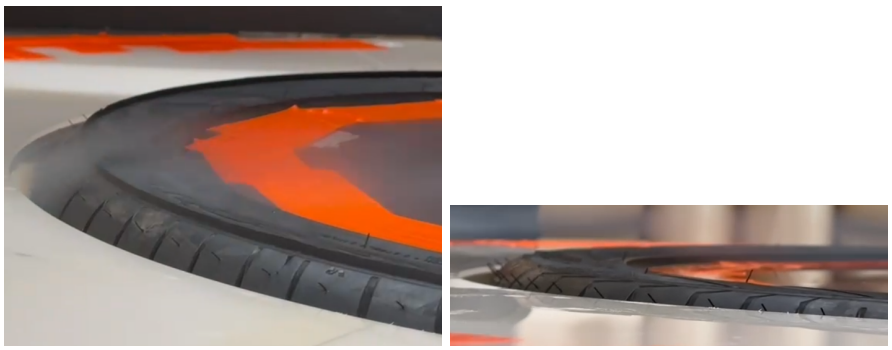

(a) Tire 3, added flash (b) Tire 4, no flash

Figure 2.1: The medium-sized tires

[1] flash: a small strip of rubber around the entire sidewall of the tire, which remains after production

The large tires as seen in Fig. 2.2 feature four distinct textures, ranging from rough and straight (Fig. 2(a)) to very smooth (Fig. 2(d)). Roughness refers to the degree of unevenness of a solid material that fall between the size scale of its shape or waviness and the finer scale of crystal lattice imperfections [18]. In the context of the given tires, the level of roughness corresponds to the potential for interaction between the tire surface and the surrounding air. The tires, ordered by texture roughness, are: Tire 7 > Tire 5 > Tire 6 > Tire 8.

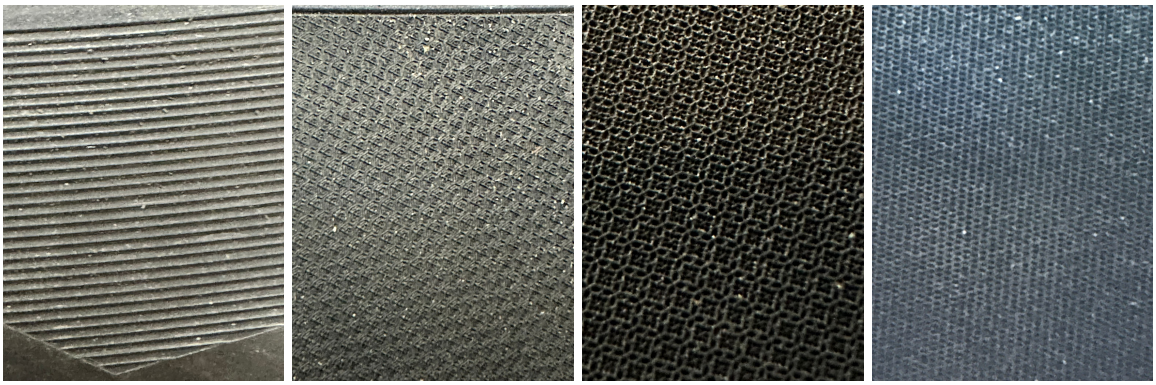

(a) Texture on tire 5 (b) Texture on tire 6 (c) Texture on tire 7 (d) Texture on tire 8

Figure 2.2: The different tire textures of the large tires. Their effect on the drag coefficient will be evaluated.

Each tire will be evaluated at six different airflow speeds: 0km/h, 42km/h, 64km/h, 86km/h, 109km/h, and 130km/h. These speeds were predetermined by the tire company Apollo [17]. An overview of the different tire names and their corresponding reference numbers is provided in Table 2.2.

Tire Name	Tire Number
XGF_BF70A18K1	1
XGF_BF70A18K3	2
XEF_CA23_115	3
XEF_CA23_114 (without flash)	4
XEF_E23305A	5
XEF_E23306A	6
XEF_E23307A	7
XEF_E23308A	8

Table 2.2: Tire names and reference numbers [17]

2.2 Theory

When measuring the flow over a certain object, it's important to consider the influence of different flow regimes and boundary layers. In this case, the area of interest is air moving across the sidewalls of the tires, which can be approximated as a flat plate with a specific drag coefficient [16] (See Fig. 2.3). Given the need for a precise measurement setup, understanding the range of forces involved is crucial. This helps in accurately determining the drag coefficient, influenced by the various textures and tire designs. Theoretical equations will provide insight into required setup specifics and measurement ranges, crucial for estimating expected forces around the tires.

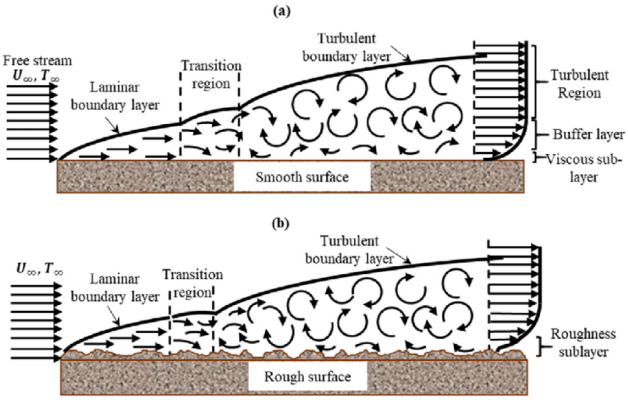

Figure 2.3: Flow regime along smooth and rough surfaces [12]

The main interest of this thesis is the skin friction drag coefficient. This coefficient is typically expressed as [9]:

$$C_{d_f} = \frac{2F_d}{\rho V_\infty^2 S_{ref}} \tag{1}$$

Where:

- C_{d_f} = skin friction drag coefficient
- F_d = skin friction drag force in N
- ρ = air density in kg/m^3
- V_∞ = far-field air speed in m/s
- S_{ref} = reference surface in m^2

To determine the theoretical expected skin friction drag coefficient, the first step is to determine the flow regime by calculating the Reynolds number. For a critical Reynolds number, which is the Reynolds number at which the boundary layer flow changes from laminar to turbulent, of $Re_c < 3.2 \cdot 10^5$ [19], the flow over a flat plate is known to be laminar. However, as the critical Reynolds number is dependent on the experimental conditions, a range is provided: $3 \cdot 10^5 < Re_c < 3 \cdot 10^6$ [19]. The equation for calculating the Reynolds number for a characteristic length, in this instance, the diameter of the tires, is defined in Eq. 2 [19].

$$Re_L = \frac{\rho V L}{\mu} \tag{2}$$

Where:

- Re_L = Reynolds number
- ρ = air density in kg/m^3
- V = air flow speed in m/s
- L = characteristic length in m
- μ = air dynamic viscosity in $kg/(m \cdot s)$

The flow regime is determined for the most extreme scenario to estimate the maximum expected Reynolds number, as seen in Eq. 3. This involves selecting the highest air speed (130km/h) and the largest characteristic length (695.9mm). As mentioned in Chapter 2.1, the wind tunnel is kept at around 22°C. Thus, material properties are scaled appropriately [20] when calculating the Reynolds number:

$$Re_L = \frac{1.196 \cdot 36.11111 \cdot 0.6959}{18.22 \cdot 10^{-6}} = 1.6495 \cdot 10^6 \tag{3}$$

This Reynolds number is within the laminar boundary layer flow regime range [19], thus it is assumed the flow over a flat plate for the given airspeeds will remain in the laminar regime. Using Blasius solution, which describes the velocity profile for a laminar boundary layer over a flat plate [10], the following relation between skin friction drag coefficient and Reynolds number in the laminar regime is found [8]:

$$C_d = \frac{1.328}{\sqrt{Re_L}} \tag{4}$$

It should be noted that it is also possible that the addition of the tire textures will cause the flow regime to be turbulent. Therefore, the turbulent relation is also provided. Unlike the laminar solution derived from the Blasius equation, this relation is based on empirical correlations [6][7][11].

$$C_d = \frac{0.045}{Re_L^{0.16}} \tag{5}$$

These relations give the following theoretical flat plate drag coefficients:

Flow regime	Theoretical drag coefficient
Laminar flow	0.001034
Turbulent flow	0.0052868

Table 2.3: Theoretical drag coefficients for different flow regimes

The expected drag force can be calculated by rewriting Eq. 1:

$$F_d = \frac{1}{2} C_{d_f} \rho V_\infty^2 S_{ref} \tag{6}$$

For laminar flow regime this is:

$$F_{d_{laminar}} = \frac{1}{2} \cdot 0.001034 \cdot 1.196 \cdot 36.1111^2 \cdot 0.38035 = 0.30668N \tag{7}$$

For turbulent flow regime this is:

$$F_{d_{turbulent}} = \frac{1}{2} \cdot 0.0052868 \cdot 1.196 \cdot 36.1111^2 \cdot 0.38035 = 1.56804N \tag{8}$$

Since these drag forces are theoretical estimations for a flat plate, they only serve as a rough estimate of the minimum forces the setup should be able to detect. As the tires are more rough and textured than the flat plate, it is expected that these drag forces are higher.

2.3 Research questions

For this research, there are two main research questions, formulated by Apollo [17].

1. What is the effect of different tire textures on the overall skin friction drag coefficient of the tire?
2. What is the effect of the flash on the overall skin friction drag coefficient of the tire?

2.4 Hypothesis

1. It is expected that the different tire textures on the side wall will have little to no effect on the overall drag coefficient of the tire. The pressure drag that could be caused by different tire designs, would be of bigger influence. In the grand scheme of things, when looking at the tire as a whole, the different tire textures are assumed to not make any difference to the overall performance of a car. However, when solely looking at the different textures of the sidewalls, it is expected that the rougher and more texturized the texture, the higher the associated drag force would be.

2. The addition of the flash is anticipated to have a bigger impact on the tires' skin friction drag coefficient. It is expected that the flash will disrupt the airflow, leading to the formation of high- and low-pressure zones, thereby introducing pressure drag. This pressure drag will combine with the skin friction drag generated by the tire textures, resulting in a greater overall impact on the skin friction drag coefficient.

3 Design Considerations and Methodology

The research aims to study the impact of different tire sidewall textures on the measured skin friction drag coefficient. Therefore, the measurement setup used for this research aims to isolate and measure only the skin friction drag caused by these textures, ensuring no other influences have to be accounted for. To accurately measure the force exerted on the top of the tire by passing air, a one-degree-of-freedom (1-DOF) system is needed, as the airflow is unidirectional, and the measurement setup should only permit movement in this direction. A mass-spring system with leaf springs is well-suited for this application, as it inherently restricts motion to a single direction [21]. Additionally, a mass-spring system is straightforward to implement and can provide precise and repeatable measurements in the controlled environment of the wind tunnel. From here on forward, this mass-spring system will be referred to as "the system" or "the setup".

To ensure that no other influences affect the measurements and only skin friction drag is measured, the setup must withstand other forms of drag and countervailing forces. This means preventing the formation of pressure drag and eliminating torsional forces in directions away from the airflow.

Given the small range of forces that will be measured, as seen in Chapter 2.2, the setup also needs to be capable of taking precise and accurate measurements, even for minimal displacements. Therefore, it is crucial that the setup provides a stable and robust basis for measurements. This entails restricting vibrations and ensuring that the airflow passes solely over the tires, without any gaps or crevices for air to escape. Finally, since there are different tire sizes with different textures and designs, it is important that each measurement is done under consistent conditions. This means positioning the axis of the tire the same way for all tires and ensuring that the height at which the tire extends from the table of the wind tunnel is consistent. The different design considerations and decisions are shown more concisely in Fig. 3.1.

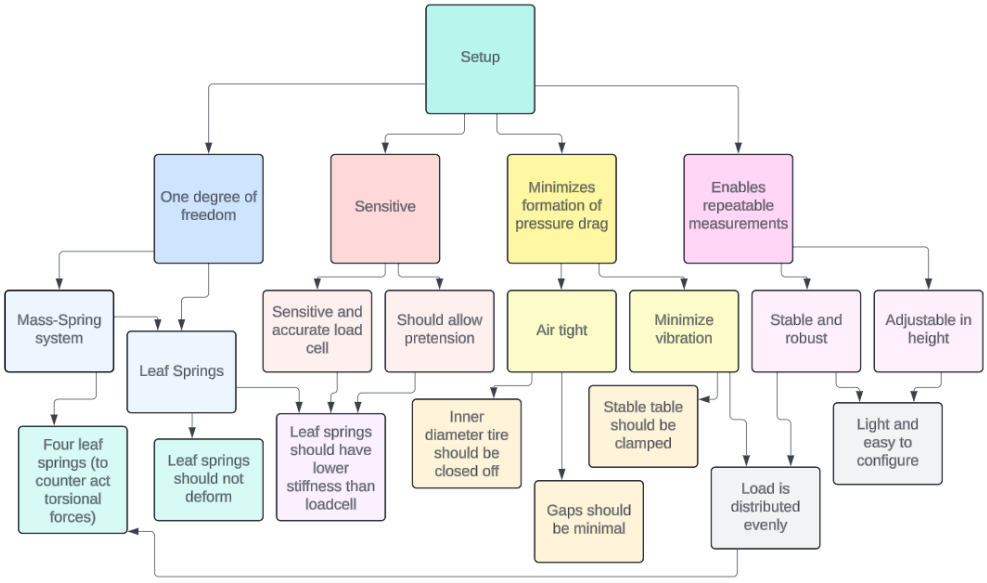

Figure 3.1: Flow chart of design considerations

3.1 Moving table

The measurement setup consists of two critical components: the mass, represented by a moving table, and the springs. The setup should be stable and sturdy enough to support the heaviest tires, which weigh up to approximately 25kg. The design must also be optimized to minimize weight and material costs while ensuring maximum strength, as the table is supported solely by leaf springs. Blocan pieces are chosen for the construction of the moving table due to their strength and ease of assembly [22]. The moving table is constructed from three 720x40x40mm Blocan, pieces connected to two 1400x40x40mm Blocan pieces. These dimensions provide ample support for the tires and sufficient space for attaching the leaf flexures. See Fig. 3.4 for the final design. The weight of the moving table was determined to be 3.12 kg.

As the main goal of the setup is to only measure the influence on skin friction from the textured sidewalls of the tire, the moving table should be height-adjustable to accommodate the varying tire heights. This ensures that only the textured outer sidewalls, as seen in Fig. 1.2, of the tires are exposed to the air flow.

Finally, to ensure a consistent examination of various tire sizes and textures from a uniform position, the tires are securely clamped at their center axis. This is achieved by positioning a rod in the middle of the moving table and securing the tire with a precisely fitted piece of hard plastic, which features a threaded hole for clamping (See Appendix A.3 Fig. A.3). The 'clamping piece'[2]is then fastened down by a nut.

3.2 Leaf springs

The second main component of the measurement setup is the springs. The springs of this mass-spring system serve several crucial functions. The first is to constrain the system to a unidirectional movement, allowing motion in only one direction while preventing rotational, torsional, and lateral movements. Additionally, the springs must support the weight of the tire.

To accommodate these needs, leaf springs were chosen due to their specific advantages. Leaf springs are particularly beneficial in providing directional stability, as they are designed to flex primarily in a single plane, thereby restricting motion in other axes and minimizing rotational and lateral movements [21], which could interfere with the accuracy of the drag force measurements. Furthermore, leaf springs have the ability to damp possible vibrations, which are introduced by the high-speed airflow in the wind tunnel [3][21][23].

While the primary purpose of the leaf springs is to only allow displacement in one direction, they should be able to do this while supporting the weight of the tires. To achieve these objectives, each corner of the moving table is equipped with a leaf spring (See Fig. 3.4). These four leaf springs collectively help prevent torquing due to torsional forces, as well as distributing the total load evenly. To secure the leaf springs to the moving table and the static part of the system, a clamping module is made. The leaf springs are clamped down for 10mm on both sides and secured by a screw in the center of this 10mm to ensure the system remains free of torque, and no deformation occurs within the springs. The clamped portion of the spring is accounted for in the spring length calculations.

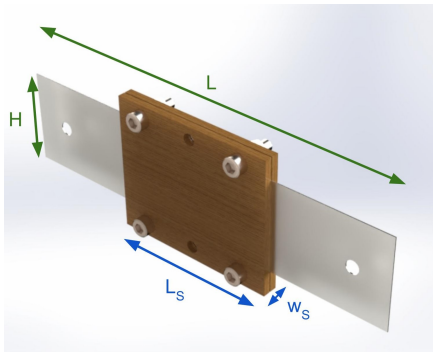

Figure 3.2: Model of the leaf springs used in the setup

Name	Length (mm)
L	140
L_S	90
W	0.5
W_S	8
H	50

Table 3.1: Dimensions of the four leaf springs

Buckling, which is the sudden deformation of a structure under load, in this case, a leaf-spring under load, can be a concern for longer leaf springs [24]. Therefore, it is crucial to find the appropriate ratio between stiffness and length. The final length of the leaf springs was determined to be 140mm [25]. To further prevent buckling, the middle 90mm of each spring is reinforced with wooden plates, as seen in Fig. 3.2. As the primary purpose of the setup is to measure the displacement of the system due to texture roughness, the leaf springs should have a minimal stiffness compared to the measuring device, ensuring all force effects are measured. The four leaf springs together have a stiffness of 2460N/m. This is validated using a physical test. The mass-spring system was rotated 90 degrees to move freely by gravity, and the displacement u of the leaf springs was measured. Then, using the spring constant equation $k = g\frac{m}{u}$, with m the mass of the moving table and g the gravity constant, the combined stiffness was calculated.

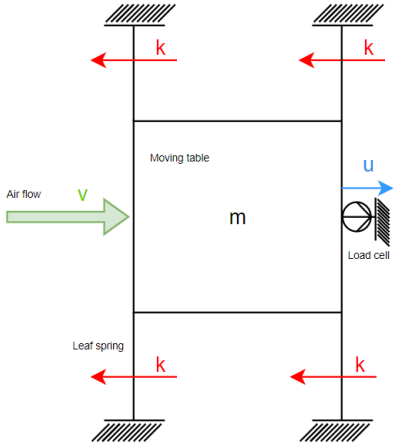

Figure 3.3: Schematic overview of the 1-DOF system

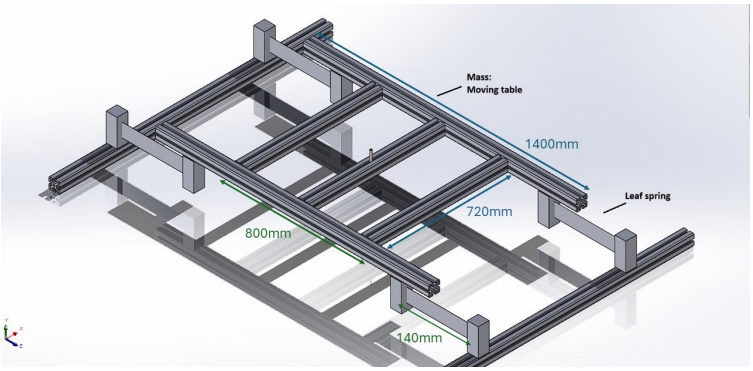

Figure 3.4: SolidWorks model of final mass-spring system

3.3 Load cell

To determine the drag coefficient of different tire textures, a load cell is used. As discussed in Chapter 2.2 and seen in Eq. 7 and Eq. 8, the expected range of force that has to be measured is very small, thus the load cell used should be capable of measuring low force ranges and small force differences.

For this reason, ultra-low-capacity (ULC) load cells are considered. ULC load cells are known for their high sensitivity, accuracy, and precision in low-force ranges [26][27]. Part of this can be attributed to their low electrical noise, and high Signal-to-Noise Ratio (SNR) [27]. This combination means that the measured force signal is significantly stronger than the background noise, enhancing its clarity and ease of interpretation. Additionally, ULC load cells are specifically engineered to accommodate low-force ranges, thereby reducing the risk of overloading [27]. A drawback, however, is that these ULC load cells are not produced in the Netherlands, which means that shipping fees and, more importantly, shipping time need to be accounted for.

Alternatively, a digital force gauge is a viable option. A digital force gauge converts mechanical force into an electrical signal, which is then displayed [28]. This conversion is done using the Wheatstone Bridge circuit, as seen in Fig. 3.5. These force gauges offer high-resolution measurements of minute forces [28][29]. Furthermore, digital force gauges integrate a built-in signal reader and amplifier, eliminating the need for additional equipment [29]. Advanced digital force gauges can also log and store data over time internally, which could potentially eliminate the need for external data-reading software [29]. The downside of these digital force gauges, however, is their costs. Most are in the price range of €150 to €250.

[2]clamping piece: a precisely fitted piece of polycarbonate, which is positioned down the center axis of a tire and clamped down using a nut and a threaded rod in the middle

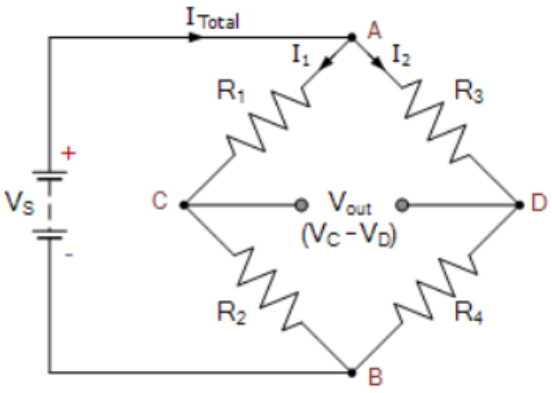

Figure 3.5: Wheatstone Bridge circuit

For optimal cost-effectiveness and time-efficiency, load cell type CB17-1K-11 (See Fig. 3.6 and Appendix A.2) is used, as it was available at the wind tunnel facility. Similar to the digital force gauge, these load cells work using the Wheatstone Bridge circuit (See Fig. 3.5). After mechanical excitation, it produces a voltage difference, denoted as V_{out}. This particular load cell has a rated capacity of 9.807N [30], which aligns well with the requirements for the setup. The recommended excitation of the load cell is 10V or less, meaning that, if calibrated correctly, each volt measured would translate to 1N of force, giving a ratio of 1:1. Additionally, the load cell has a stiffness of 57.69kN/m [30], which is indeed larger than that of the leaf springs, as discussed in Chapter 3.2.

To accurately measure the forces induced by varying wind velocities, the load cell is placed transversely to the movement of the leaf springs. Placing the load cell in the center of the measurement setup ensures the voltage difference measured is not influenced by possible torsional forces within the system. The setup is configured to channel all forces acting on the system through the load cell, which is securely mounted to the moving table and pre-tensioned to ensure continuous contact throughout the measurements.

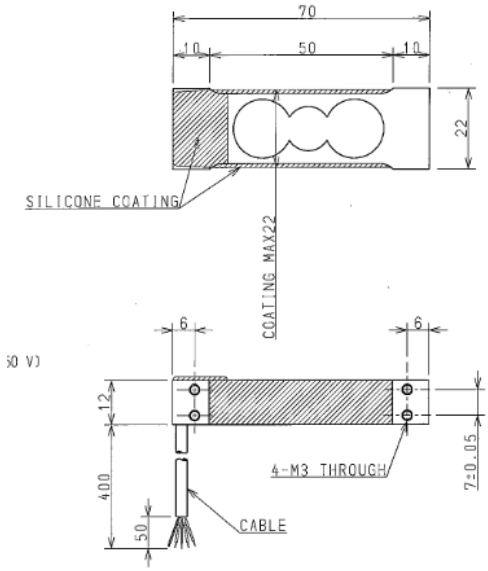

Figure 3.6: Load cell used (CB17-1K-11) [30]

3.4 Minimizing pressure drag

One of the most important roles of the design is minimizing the opportunity for pressure drag to occur, as the focus of the setup should solely be on the skin friction drag. To achieve this, it is essential to eliminate room for any high- or low-pressure zones in the setup. This is accomplished through various means, with the primary method being the closure of any gaps in the setup. The first major gap to address is the empty ring of the wind tunnel. The wind tunnel includes two removable discs, one at the top and one at the bottom (see Fig. 3.7). The bottom one of these is removed, as this is where the tires will be positioned. However, these removable discs have a diameter of 1197.1mm, whereas the largest tire outer diameter is 695.9mm. Therefore, a 'gap-sealing ring'[3] should be made to close this gap.

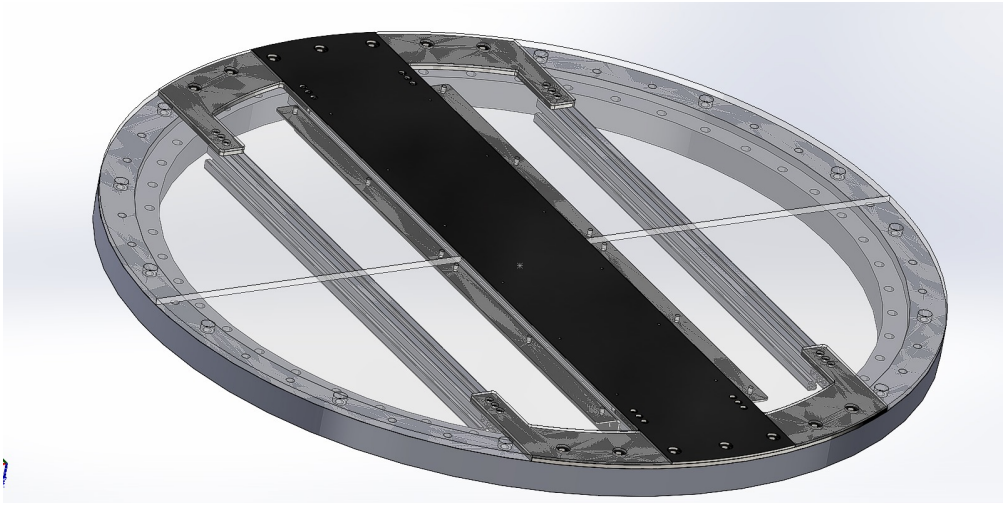

Figure 3.7: SolidWorks model of the removable disc of the wind tunnel table

The cutting capacities of the machinery [the laser-cutter Speedy400] are limited to a maximum area of 1016x610mm [31]. Consequently, a circle with an outer diameter of 1197.1mm can not be cut in a single operation. For this reason, it is chosen to split the ring into four quarters. However, this introduces a new challenge. As the gap-sealing ring is meant to act as nothing more than an extension of the actual wind tunnel table, its introduction should not allow for any vibrations or deformations to occur. It should be a stable, complete circle without any weak points. If a weak point were to occur, the gap-sealing ring could break, causing damage to the wind tunnel and interfering with measurements.

To achieve this, a two-layer design was selected. The bottom layer is composed of 6mm thick plywood, known for its excellent vibration damping properties [32], while the upper layer is made of 5mm thick acrylic, which is stiff and smooth, minimizing friction drag influence [33]. Together the two layers are 11mm thick, which is the thickness of the removable disc (Fig. 3.7). The combination of these materials ensures the gap-sealing ring is both rigid and vibration-dampening, reducing the risk of breakage.

Other materials considered for the gap-sealing ring included aluminum and polycarbonate. Aluminum, while very strong and lightweight [34], was decided unfit for this setup due to its lack of inherent vibration-damping properties [34], which could have led to less accurate measurements. It is also harder to work with [34]. Polycarbonate, known for its durability and impact resistance [33], was another option. However, its cost was significantly higher compared to plywood and acrylic, and its surface smoothness did not offer any substantial advantage over acrylic. For these reasons, the plywood and acrylic combination provided the best balance between mechanical properties, minimization of friction drag, and cost-effectiveness.

[3] gap-sealing ring: a circle made to eliminate the space between the outer diameter of the removable disc and the tire

To further enhance stability, the acrylic layer is rotated 45 degrees relative to the wooden layer, offsetting the 'break lines', which are the small gaps where the quarters meet. This design minimizes the likelihood of failure at these junctions. To further eliminate vibrations and possible gaps, the quarters of both layers are secured together using double-sided tape, and fastened together with countersunk screws and nuts at the bottom. The outer diameter is securely clamped to the stable wind tunnel table with 10mm thick screws. The final design of the gap-sealing ring is shown in Fig. 3.8.

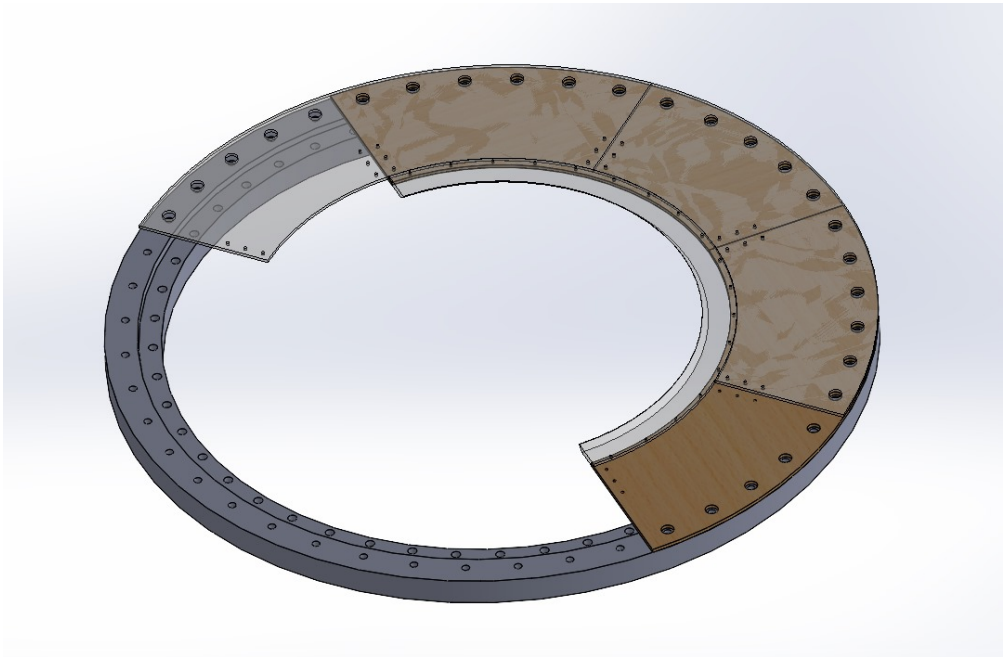

Figure 3.8: SolidWorks design of the gap-sealing ring

As there are three different tire sizes, and the gap-sealing ring has a set dimension, a gap remains between the gap-sealing ring and the actual tire. To address this, an 'outsert'[4], as seen in Fig. 3.9, is created for each size. These outserts connect to the gap-sealing ring. The upper acrylic layer of the gap-sealing ring has an inner diameter that is 10mm smaller than that of its corresponding wooden layer, creating a ridge that ensures the outserts can be easily connected. The space between the outsert and the actual tire is small enough to prevent the occurrence of pressure drag while allowing room for the tire to move. The inner diameter of the outserts is chamfered - sloped cuts on the edges - to ensure that air flows smoothly past the tire and outsert, preventing pressure drag influences or disturbances in airflow. The outer diameter of the outserts is milled to an edge of 5mm thick and 10mm wide, enabling a strong, well-fitted connection to the gap-sealing ring (See Fig. 9(b)).

[4]outsert: two acrylic half rings cut to eliminate the space between the inner diameter of the gap-sealing ring and outer diameter of the tire

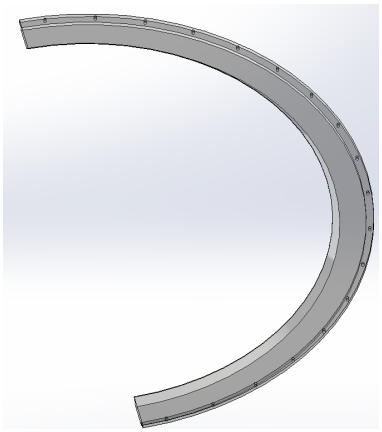

(a) Topview of the outsert ring

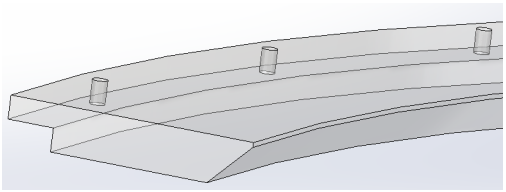

(b) Sideview of the outsert ring, chamfered and with an edge

Figure 3.9: SolidWorks design of an outsert ring

Another area that must be closed off is the inner diameter of the tire itself. Given the three different tire sizes, three different 'inserts'[5] are required. For the inserts, 10mm thick acrylic was chosen, as it was the thickest material that could be cut by the available laser cutter. The thickness ensures minimal vibrations [33], and the acrylic layer itself is smooth enough to assume it will have close to no influence on the measured drag coefficients - as will be proven later in Chapter 4.3.

The inner diameter of the tires must be determined precisely to ensure a perfect fit for the insert. The insert's outer diameter is cut to 3mm smaller than the measured inner tire diameter. A small rubber elastic band is then taped to the outside of the inserts to ensure a complete seal between the insert and the tire, similar to the seal of a mason jar lid.

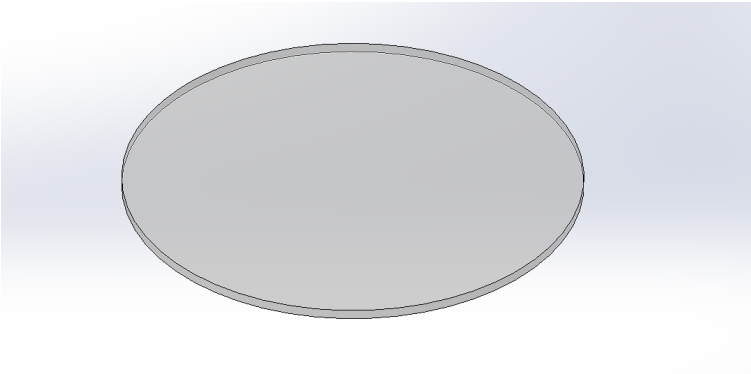

Figure 3.10: SolidWorks model of the insert, before attaching a rubber band

Additionally, tape was used on the gap-sealing ring, the inserts, and the outserts to ensure the elimination of any gaps that could affect the measurements.

Small	444.1mm
Medium	467.5mm
Large	492.9mm

Table 3.2: Diameters of the inserts

[5]insert: an acrylic circle made to eliminate the gap within the inner diameter of a tire

3.5 Data analysis

The last step involves data gathering and analysis. Each tire is measured three times at six different speeds, ranging from 0 to 130km/h. The selected speeds for evaluation are 42km/h, 64km/h, 86km/h, 109km/h, and 130km/h. For every speed, the load cell's output is in voltage difference, which, after proper calibration, accurately represents the force exerted on the load cell. A Multi-Channel Compact Amplifier is used to read the data. Calibration is done using various sets of weights, applying force to the load cell, and adjusting the Multi-Channel Compact Amplifier to achieve a 1:1 ratio. Matlab is used for further analysis. The data is normalized to ensure all plots begin at 0.

3.6 Setting up the wind tunnel

It is essential to set up the wind tunnel properly to ensure reliable results. First, the gap-sealing ring is assembled (See Fig. 3.8). The wooden quarters are joined to form a circle, and then the acrylic quarters are arranged on top, offset by 45 degrees. Double-sided tape is placed between the two layers to ensure they remain securely together during testing, preventing any gaps that could allow wind to pass through and potentially cause damage. Once both circles are correctly aligned, countersunk screws are inserted from the top and tightened from the bottom with nuts to fully secure the entire gap-sealing ring.

Next, this gap-sealing ring is positioned within the wind tunnel table and clamped down throughout its full outer edge, with 1mm thick spacers underneath. This ensures that the 10mm thick gap-sealing ring is at the same height as the 11mm thick removable disc (See Fig. 3.7), making it completely level with the wind tunnel table. The mass-spring system (See Fig. 3.4) is put on a jack, which forms a stable basis to secure the set-up in place.

The tire is then placed in the center of the moving table and clamped down using the threaded piece of plastic and a nut. Once the tire is securely fastened, the appropriate insert (See Fig. 3.10) is put in the tire to close off the inner diameter. After making sure the insert is at the right height across the entire diameter of the tire, the table with the tire is adjusted to the right height, meaning only the outermost part of the tire is exposed to the wind.

Next, the leaf springs are inspected and tightened, ensuring they are not under any tension, which could cause buckling and deforming. Each leaf spring can be slightly adjusted in height, to make sure the whole setup is level. Once leveled, the outserts (See Fig. 3.9) fitting the tire dimensions are connected to the gap-sealing ring to close off any extra space between the tire and the gap-sealing ring. Finally, the wind tunnel will be closed off from any outside influences and turned on. A final schematic overview is given in Fig. 3.11.

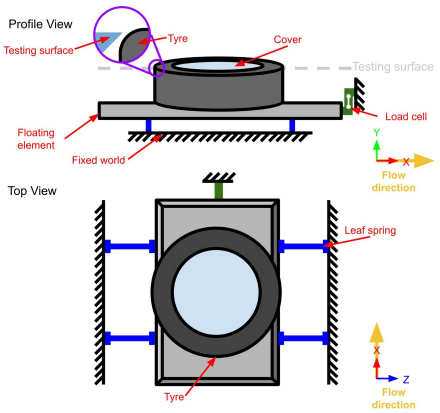

Figure 3.11: A schematic overview of the measurement setup, highlighting the different elements

4 Results and Discussion

4.1 Raw data

After setting up in the wind tunnel and collecting the data, attention turns to analyzing the results. The primary focus is on evaluating how the addition of the flash impacts the skin friction drag of the medium tires, as shown in Fig. 4.3 and Fig. 4.4, and how different textures affect the drag coefficient of the large tires, shown in Fig. 4.5, Fig. 4.6, Fig. 4.7, and Fig. 4.8.

First, the raw data is plotted to get an idea of the behavior of the system.

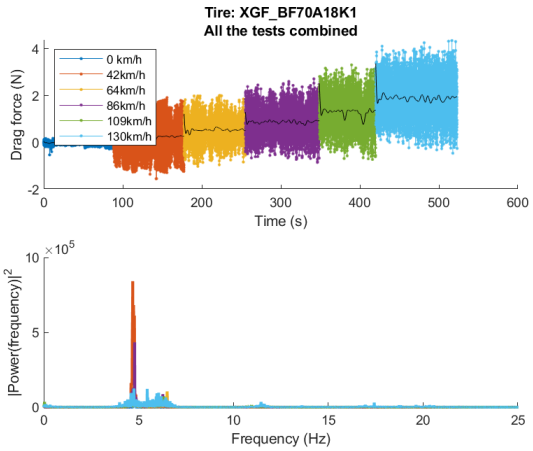

Figure 4.1: Raw data of small tire 1

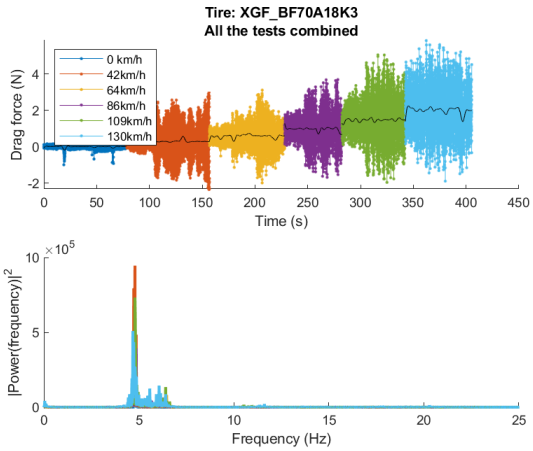

Figure 4.2: Raw data of small tire 2

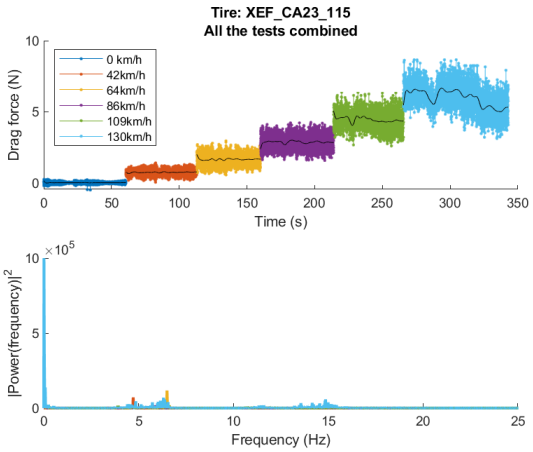

Figure 4.3: Raw data of medium tire 3

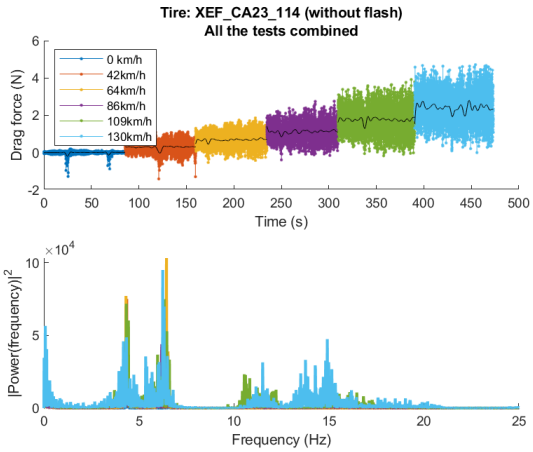

Figure 4.4: Raw data of medium tire 4

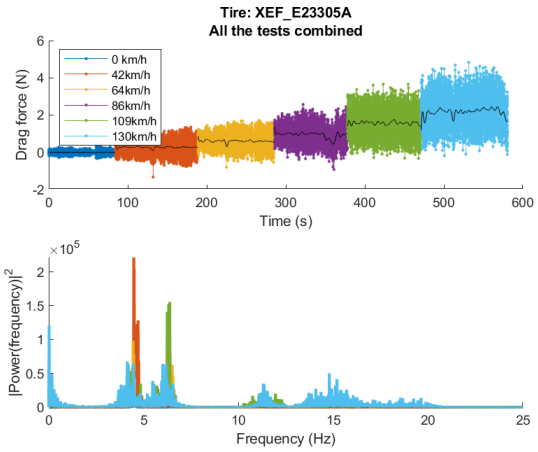

Figure 4.5: Raw data of large tire 5

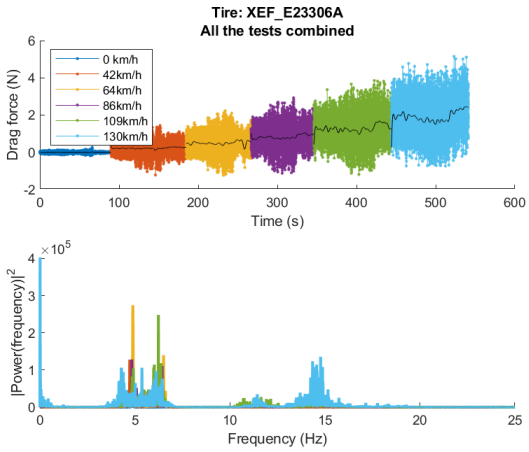

Figure 4.6: Raw data of large tire 6

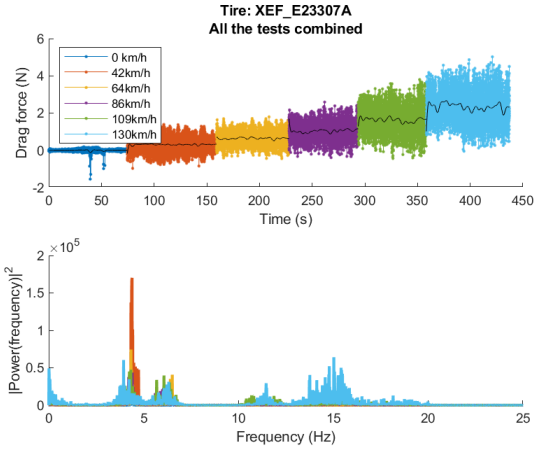

Figure 4.7: Raw data of large tire 7

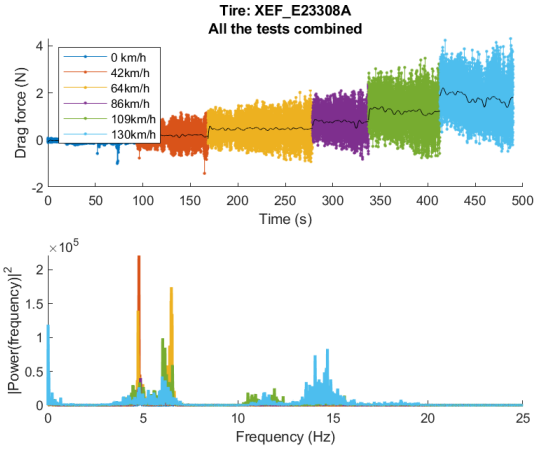

Figure 4.8: Raw data of large tire 8

From the raw data, a few things stand out. When examining the plots, a consistent trend is evident: as the airspeed increases, the drag force also increases. This outcome is expected because a higher air flow speed means more air is displaced [9], and thus a higher force acts on the tire. This is a good indication that the setup functioned correctly.

Another noticeable trend in most plots is that the variance of measurements increases with air speed. This could be attributed to several factors. The most likely cause is that the laminar airflow is disturbed by the addition of the tire side walls, leading to a boundary layer effect [15], as seen in Fig. 2.3. At higher speeds, this boundary layer can transition from laminar to turbulent flow [10][15], which is thicker and more chaotic, thus leading to more interactions between air and tire. These interactions, in turn, cause frictional forces [11], which can result in greater variability in the measured skin friction drag.

Another possible factor is the dynamic response of the load cell. A load cell has a distinct response time, which is the time it takes for a load cell to react to changes in force [35]. At higher airflow speeds, the drag forces can change rapidly due to the changes in airflow turbulence [9]. For a load cell with a lower response time, these rapid changes cannot all be registered, which causes discrepancies in the measured forces.

Similarly, the frequency response of a load cell is influential, determining the range of frequencies at which a load cell can accurately determine rapid changes in force [35]. At higher speeds, these changes in force could be larger. A load cell with a limited frequency response may not register these rapid changes, leading to further discrepancies in the measured forces.

Despite the large variance in measurements, there is still valuable data to examine. To get a clear picture of the behavior of each tire for different flow speeds, the mean value is plotted, depicted as the black line in the drag force plots. This black line is the mean value of three different tests and provides a useful way to compare the overall performance of different tires.

When comparing Fig. 4.3 and Fig. 4.4, the difference between the flash around the tire and no flash becomes very clear. Tire 4 shows a small but noticeable increase in drag force per air speed setting, while tire 3 shows a significant step increase for each change.

Additional to the change in drag force over time for different air speeds, the raw data sets were used for a frequency analysis through Fourier transforms. This analysis gives insights into the natural oscillation frequency of the measurement setup, known as the eigenfrequency [35]. The eigenfrequency is consistent for all tires, with frequency plots indicating a range between 4.5Hz and 6.5Hz. When looking at Figures 4.4, 4.5, 4.6, 4.7 and 4.8 a second peak at around 15Hz can be seen. This peak is caused by a harmonic of the eigenfrequency [35]. This means that it is a multiple of the eigenfrequency, at 5Hz. In Figures 4.3, 4.4, 4.5, 4.6, and 4.8 a third peak at 0Hz can be observed. These peaks can be attributed to the offset. This offset comes from the mean value of the measurement signals [35]. When a mean value of a time-domain signal is shown in a plot, it is represented by a peak at 0Hz [35]. Each different airflow speed will have a peak at 0Hz due to its specific mean value.

For future reference, it is recommended that the x-axis for each raw data plot is the same. This standardization improves the comparability between different plots, making them easier to interpret. The current inconsistency between the different plots is because the air speed was manually adjusted after periods of 20-30 seconds. To improve comparability, it is advisable to use a stopwatch to ensure each air speed is measured for the same amount of time.

4.2 Validation test

To account for the effect of the acrylic inserts (See Fig. 3.10) within the inner diameter of the tires on the overall measured drag force and to validate the measurement setup, a validation test is conducted using a flat plate made of the same material (See Fig. 4.9). This flat plate is designed to match the dimensions of the largest tire.

Blasius equations, which describe the behavior of fluid flow near a flat plate, were used to plot theoretical flat plate drag coefficients for laminar and turbulent flow alongside the validation test results, as seen in Fig. 4.10. This plot confirms the assumption in Chapter 2.2 of a predominantly laminar flow regime for the flat plate. More importantly, this flat plate test clearly shows a linear relation between the wind speed and the drag force. Therefore the setup can be considered validated, as this result aligns perfectly with expectations. The combination of these theoretical approximations and the validation test also makes it possible to determine the influence of the tire inserts on the overall drag force measurements, as the inserts are made from the same material and share the same properties.

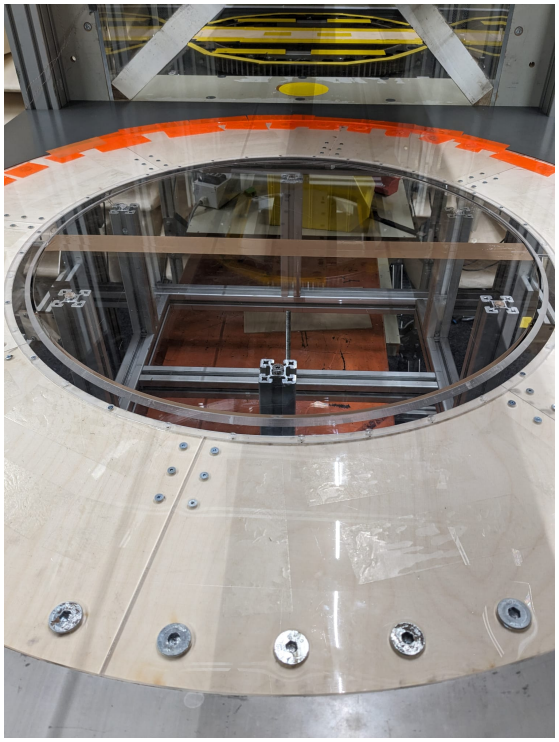

Figure 4.9: Test setup for the flat plate validation test

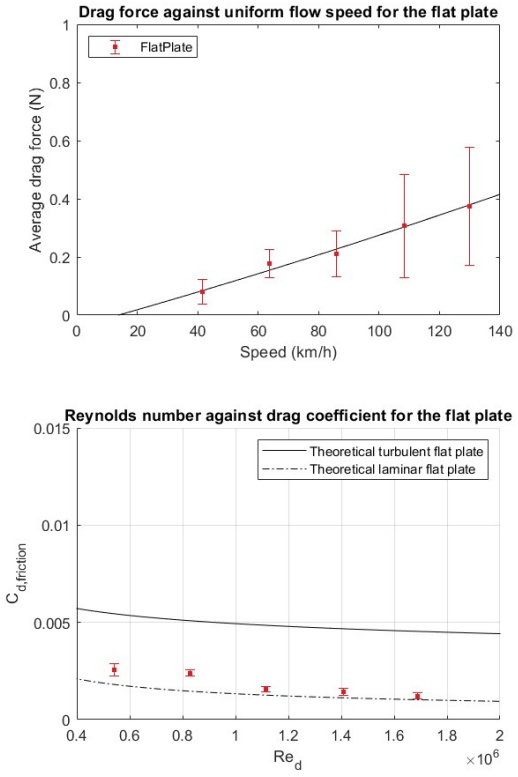

Figure 4.10: Drag force of the flat plate validation test

4.3 Tires

Finally, the average drag force and the corresponding drag force coefficients of the tires are plotted.

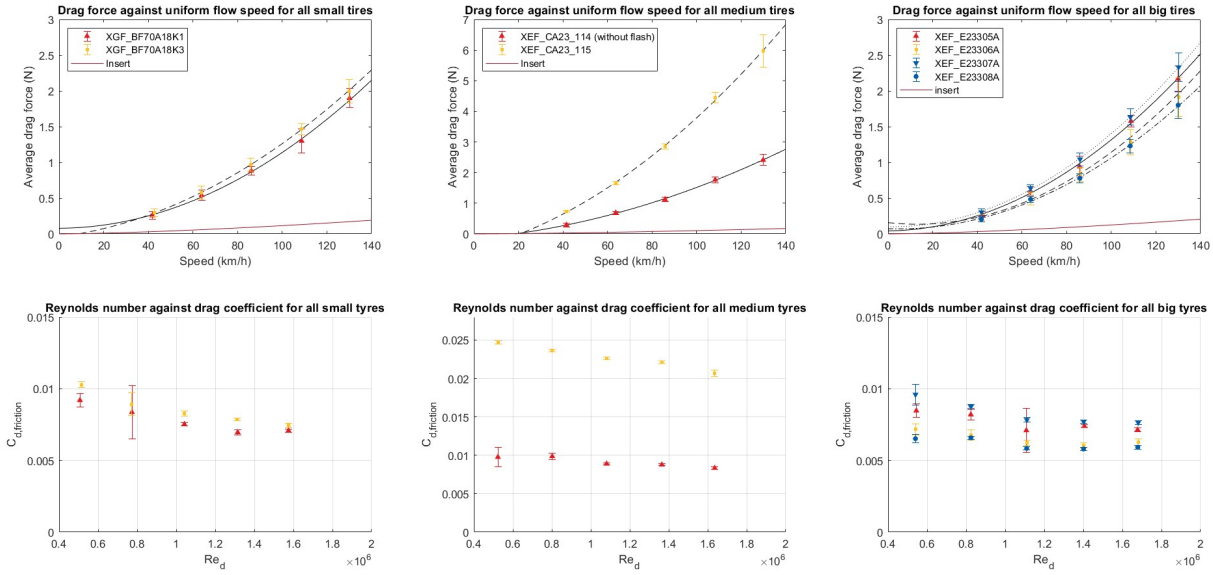

(a) Small tires (b) Medium tires (c) Large tires

Figure 4.11: Plot of the average drag force and the skin friction drag coefficient

4.3.1 Small tires

When analyzing the results of the small tires, it is important to note that both tires have very similar textures, so their performance is expected to be very close. As can be seen from Fig. 11(a), this is the case. When looking at the total average drag force exerted on the tires and the average drag force caused by the insert within this tire, it can be concluded that the insert only makes up a small margin of the overall measured drag force. This is positive, as it means the inserts do not affect the outcome of the measured skin friction drag coefficients much, which aligns with the specific properties of the chosen acrylic insert.

Additionally, the relationship between air speed and the average drag coefficient is evident. The higher the flow speed, the bigger the average drag force measured. When looking at Eq. 6, it is clear that the drag force is proportional to the square of the airflow velocity V_∞. Thus, as the air speed increases, the drag force increases quadratically. The plot in Fig. 11(a) shows this same relationship, confirming that the setup worked accordingly.

Another important aspect is the determined drag coefficient. As can be seen clearly in Fig. 11(a), the skin friction drag coefficient decreases as the Reynolds number increases. Reynolds number increases for higher flow velocities or larger characteristic lengths (See Eq. 2). When this flow velocity increases, the relative influence of the friction forces due to the internal friction of a fluid through its viscosity decreases, which causes lower drag coefficients [4]. This trend aligns with the drag coefficient Eq. 4 and Eq. 5, where the Reynolds number is in the denominator.

To get a more complete picture of the drag coefficients of the small tires, their drag coefficients for an air speed of 130km/h, corresponding to a Reynolds number of around $1.57 \cdot 10^6$, are highlighted in Table 4.1:

Tire number	Drag coefficient
Tire 1	0.0070
Tire 2	0.0074

Table 4.1: Skin friction drag coefficients of the small tires

4.3.2 Medium tires

While the small tires do not have significant differences in texture and design, the medium tires present a different scenario. For the medium tires, the focus is on the addition of the flash (See Fig. 2.1). An additional strip of rubber around the entire surface of the tire is expected to influence its drag performance a lot, especially compared to the subtle differences in texture that are examined for the small and large tires.

When looking at Fig. 11(b), the difference in performance is immediately apparent. This difference in drag is most likely due to the occurance of pressure drag around this flash. The addition of a 'vertical wall' in the air flow will disturb the natural flow, creating high-pressure zones, and subsequent pressure drag [15] (See Fig. 1.1). Similar to the small tires, the average drag force does seem to follow an exponential relation with the air velocity for both medium tires. Another important observation is that, like the small tires, the insert contributes only a fraction to the overall measured average drag force. Finally, as for the small tires, it can be observed in Fig. 11(b) that the skin friction drag coefficient decreases as the Reynolds number increases. This is as expected.

To get a more complete picture of the drag coefficients of the corresponding medium tires, their drag coefficients for an air speed of 130km/h, corresponding to a Reynolds number of around $1.63 \cdot 10^6$, are highlighted in Table 4.2:

Tire number	Drag coefficient
Tire 3	0.0206
Tire 4	0.0083

Table 4.2: Skin friction drag coefficients of the medium tires

Based on this table, hypothesis 2, which notes that the addition of a flash is anticipated to introduce pressure drag, which greatly contributes to the overall drag coefficient, can be proven.

4.3.3 Large tires

Contrary to the small and medium tires, there are four different large tires, each with a different texture (See Fig. 2.2). When looking at Fig. 11(c) it can be observed that the tires exhibit a trend in drag force corresponding to their roughness. Specifically, in terms of average drag force, the tires rank as follows: Tire 8 $<$ Tire 6 $<$ Tire 5 $<$ Tire 7. These results align with the observable roughness of tire texture, as seen in Fig. 2.2.

Another observation from Fig. 11(c) is that the drag coefficient reduces as the Reynolds number increases. As explained in the section on small tires, this is expected. The quadratic relation between air speed and drag force is also clearly visible. Additionally, for the large tires, the effect of the insert is still minimal.

To get a better idea of the actual difference in drag force coefficient, the drag force coefficients for an air speed of 130km/h, which corresponds to a Reynolds number of around $1.68 \cdot 10^6$, are highlighted in Table 4.3:

Tire number	Drag coefficient
Tire 5	0.0071
Tire 6	0.0062
Tire 7	0.0076
Tire 8	0.0059

Table 4.3: Skin friction drag coefficients of the large tires

Based on this table, hypothesis 1, which notes that it is anticipated that the measured drag force will increase with the roughness and texture of the tire, can be proven.

4.4 Discussion of results

The measurements of the different tire sizes have provided valuable insight into the impact of various tire textures and the addition of the flash. A comprehensive overview of all the tire's performances compared to each other is not yet provided. The main focus of this research is the measured drag coefficient for each tire. When looking at Tables 4.1, 4.2, and 4.3, several observations become apparent. After arranging the drag coefficients from highest to lowest, the following ranking emerges:

Ranking	Tire size and number	Drag coefficient
#1	Medium Tire 3	0.0206
#2	Medium Tire 4	0.0083
#3	Large Tire 7	0.0076
#4	Small Tire 2	0.0074
#5	Large Tire 5	0.0071
#6	Small Tire 1	0.0070
#7	Large Tire 6	0.0062
#8	Large Tire 8	0.0059

Table 4.4: Ranking of tires and their corresponding drag coefficients at 130km/h

The tire with the added flash has the highest drag coefficient, more than twice as large as the medium tire without the added flash, which places second. This general ranking also indicates that the tire size has minimal impact on its drag coefficient, as small and large show similar performance, highlighting that the texture of the tire sidewall is the biggest determinant of its drag performance.

When zooming in on the skin friction drag coefficient plots in Fig. 4.11, certain observations stand out, that have not yet been highlighted. In Fig. 11(a), the error bar of tire 1 for the drag coefficient at a Reynolds number of $0.78 \cdot 10^6$ is a lot bigger than the other error bars. The same can be said for the error bar of the drag coefficient of tire 5 at a Reynolds number or $1.11 \cdot 10^6$ in Fig. 11(c). This suggests that there may be significant outliers within these air speeds for those tires. In general, the measurement setup gave some good and conclusive results.

4.5 What could be improved

Although the provided results were desirable, the measurement setup and process could be improved or executed differently in several ways.

For the flat plate validation test, seen in 4.2, three sizes could be used instead of one. This way, a data fit could result in a relation for the total area of the flat plate against the force outputted on the load cell. This could then be scaled to the size of the inserts within the tires, meaning an even more precise approximation of the actual drag coefficient per tire texture could be made. However, when looking at Fig. 4.10, the linear relation of the laminar flow over a flat plate does suggest that the scaling that was used in this research is a good estimation, as this behavior is as expected, and well within the theoretical laminar flow range.

Another thing that influences the measurements of the system is the leaf flexures. As the leaf flexures are put under pre-tension, its effect could influence the overall output. The overall results could be corrected, meaning that the effect of the leaf springs and of the overall used materials, which are not part of the actual tire textures, could be taken into account. However, for accurate depiction, it was chosen to show these effects in the error bars within the plots themselves.

The fact that these leaf springs are not perfect did influence the measurements. As can be seen in the raw data plots in Chapter 4.1, the system vibrates a lot. To minimize the vibrating of the system and thus provide measurement sets with a lower variance, three ways of dampening were tried.

The first method, as seen in Fig. 12(a), involved attaching a large piece of foam to the setup. The idea was that as the moving table with the tire shifted, the foam would displace air and create damping forces. However, this approach proved ineffective, when comparing the damped data to the undamped data sets.

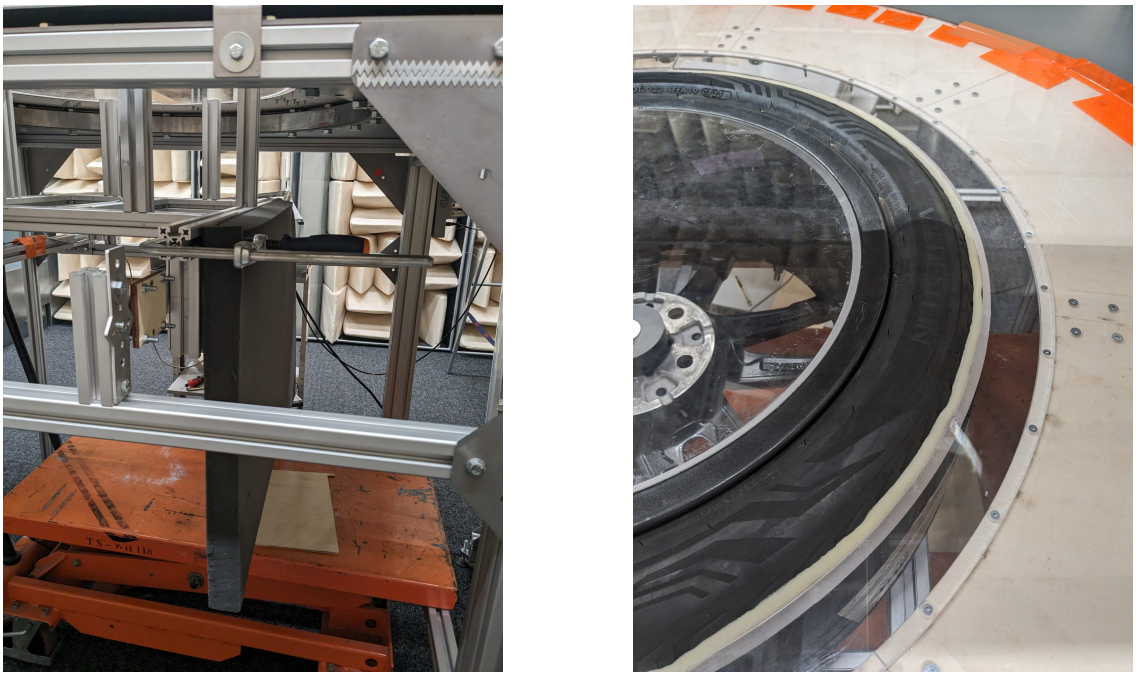

(a) Dampening method 1

(b) Dampening method 2

Figure 4.12: Methods of dampening

The second method of dampening, as seen in Fig. 12(b), was to attach a piece of foam to the tire. This was intended to reduce vibration by filling the gap between the tire and the outsert, dampening any displacements of the tire. Despite this effort, the method also did not deliver the desired results.

A third method of dampening that was briefly explored was to use weights to weigh down the setup. This also did not prove fruitful.

Another improvement could be to fully close the space between tire and outsert. Originally, this gap was intended to allow the tire some room for movement. However, since the design is centered around directing all forces through the load cell, the setup should not actually be moving in practical use. In retrospect, the deliberate but small gap may have impacted the measurements and, ideally, should not have been present.

A final improvement would be to streamline the process of setting up each tire. Currently, each tire has to be manually installed. This involves removing the insert, unscrewing the clamping part, removing the outsert, taking out the tire, putting the new tire in, clamping it down, attaching the new outsert, inserting the new insert, and adjusting the setup to the correct height. This process is tedious, with the potential to damage or disrupt the measurement system. Additionally, leveling the tire each time proved to be somewhat challenging.

To enhance efficiency, a puzzle piece-like design could be implemented to remove the need for unscrewing and screwing the outserts each time. A lifting mechanism to easily take out the tire could also cut some time and effort. Moreover, incorporating a rail system to easily adjust and securely fasten the stable part of the setup to the correct height would address the leveling and height adjustment challenges effectively.

4.5.1 Future research

To start, it is important to note that the results obtained from this measurement setup are reliable and can be used to draw conclusions. For future research, however, several improvements could be made. As mentioned earlier in Chapter 4.1, the measurements have a significant variance due to the system's vibration. Despite experimenting with three damping methods, little improvement was observed. In future research, employing a fully damped system could be beneficial. A fully dampened system would prevent vibration, ensuring that all forces are transmitted through the load cell. Due to time constraints, achieving this was not possible at this time.

Another potential adaptation for future research involves exploring different measurement methods. The scope of this research was to create a setup with a horizontal tire, where only the sidewalls of the tire were exposed to the airflow of the wind tunnel to focus on the side wall texture and flash effects [17]. However, the author would like to suggest two different methods that could possibly achieve better, more consistent results [36].

The first one is the use of hot wire anemometry. Hot wire anemometry uses a heated wire to measure the velocity of air flow, which in turn can be used to determine drag force [37]. In the case of air flow across a tire in a wind tunnel environment, the following procedure could be implemented:

1. Place the hot-wire sensor behind the tire, in the flow field of the wind tunnel. If available, use multiple sensors to map the flow profile
2. Calibrate the hot-wire sensor by setting the wind tunnel to different flow speeds and measuring with the sensor
3. Run the wind tunnel and measure at different speeds
4. Extrude the voltage output of these sensors and convert it into velocity
5. Plot the velocity profiles for different tires.
6. Determine the drag force of different tires by integrating the pressure distribution around the tires surface area

The hot wire excels in measuring small changes in velocity and provides a high-frequency response [37]. This, combined with its ease of adaptation [37], makes it a viable contender for this research. The problems with vibrations would also disappear.

A second viable solution could be the use of a Preston tube. A Preston tube measures local wall shear stress [38], which is directly related to skin friction. It does this by measuring the pressure difference between a point on, or very close to, the surface (in the boundary layer) and the static pressure in the air flow above [38]. The following procedure could be implemented:

1. Place the Preston tube very close to the tire's surface, within the boundary layer. If available, use multiple Preston tubes to map the wall shear stress distribution
2. Extrude the measured pressure difference by connecting the Preston tube to a differential pressure transducer
3. Calibrate the Preston tube using literature
4. Run the wind tunnel and measure at different speeds
5. Plot the wall shear stress data and integrate it over the surface area of the tire to get the drag force

The advantage of the Preston tube is that you measure the wall shear stress directly without having to implement a secondary measurement setup. Additionally, a Preston tube has high accuracy when it is properly calibrated, and it is easy to implement [38].

5 Conclusion

This thesis attempted to answer two research questions. The first topic of research was the influence of different sidewall textures on the measured drag force and on the skin friction drag coefficient. The second was about the influence of an additional flash around the tire on the measured drag force and on the skin friction drag coefficient. A measurement setup was made, and the results, as shown in Chapter 4.3, were desirable. Both research questions were effectively adressed.

Hypothesis 1 about the different sidewall textures is correct. The rougher the tire texture, the bigger the skin friction drag coefficient. This can clearly be seen from Tab. 4.3, when comparing to Fig. 2.2.

The flash around the tire causes more drag than the tire without. This is caused by the eddies formed behind the flash due to the disturbance in flow. This causes pressure drag to form, which influences the overall measured drag force. This aligns with Hypothesis 2, that the disruption of airflow causes more drag.

6 Acknowledgements

The author would like to express gratitude to Apollo Tyres for presenting the initial research and providing the tires used for the measurements.

The author also wants to express appreciation to Walter Lette for his continuous effort in guiding the team in the wind tunnel and always providing practical solutions. Without him, this setup and, most importantly, the measurements would not have been possible.

Finally, the author would like to express gratitude to Elise Leusink for her dedication in producing all the various components used in the setup. Without her assistance in design, material gathering, laser-cutting, and putting in long hours to help us meet our measurement deadline, this setup would not have been completed on time, and taking measurements would not have been possible.

7 Bibliography

References

[1] Z. Sun, W.A.A.S. Premarathna, K. Anupam, C. Kasbergen, and S. M.J.G. Erkens. A state-of-the-art review on rolling resistance of asphalt pavements and its environmental impact. *Construction and Building Materials*, 411, 2024.

[2] Engineering Transportation Research Board National Academies of Sciences, Medicine. 2006. Tires, and DC: The National Academies Press. https://doi.org/10.17226/11620. Passenger Vehicle Fuel Economy: Informing Consumers, Improving Performance Special Report 286. Washington. *Tires and Passenger Vehicle Fuel Economy - Special Report 286*. Transportation Research Board, Washington, D.C., 2006.

[3] John D Anderson. *Fundamentals of Aerodynamics (Mcgraw Hill Series in Aeronautical and Aerospace Engineering)*. 2009.

[4] Robert W. Fox, Alan T. McDonald, and Philip J. Pritchard. *Introduction to Fluid Mechanics. 8th ed.* Wiley, 2011.

[5] Erik Josefsson, Simone Sebben, and Magnus Urquhart. Characterisation of the flow around passenger vehicle wheels with varying tyre profiles. *International Journal of Heat and Fluid Flow*, 103:109191, 2023.

[6] Frank M. White. Chapter 7: Internal Flows and Chapter 9: External Flows. In John J. Corrigan and David A. Damstra, editors, *Fluid Mechanics - Third Edition*, chapter 7 and 9. McGraw-Hill, Inc., Brooklyn, 3 edition, 1994.

[7] Herman Schlichting and Klaus Gersten. Chapter 20: Turbulent Boundary Layers. In *Boundary-layer Theory - 8th Revised and Enlarged Version*, chapter 20. Springer-Verlag, New-York; Berlin, 8 edition, 2000.

[8] Hermann Schlichting and Klaus Gersten. Chapter 6: Laminar Boundary Layers. In *Boundary-layer Theory - 8th Revised and Enlarged Version*. Springer-Verlag, New-York; Berlin, 8 edition, 2000.

[9] Snorri Gudmundsson. Aircraft Drag Analysis. In *General Aviation Aircraft Design*, pages 661–760. Elsevier, 2014.

[10] Herrmann Schlichting and Klaus Gertsen. *Boundary Layer Theory - 8th Revised and Enlarged Edition*. Springer-Verlag, New York, 8 edition, 2000.

[11] John D. Jr. Anderson. Chapter 18: Laminar-Turbulent Transition and Turbulence. In John D. Anderson Jr., editor, *Fundamentals Of Aerodynamics 5th Edition*, chapter 18. McGraw-Hill, New-York, 5 edition, 2011.

[12] Mohammadreza Kadivar, David Tormey, and Gerard McGranaghan. A review on turbulent flow over rough surfaces: Fundamentals and theories. *International Journal of Thermofluids*, 10:100077, 5 2021.

[13] Olajide Ganiyu Akinlade. *Effects of surface roughness on the flow characteristics in a turbulent boundary layer*. PhD thesis, University of Saskatchewan, 2005.

[14] Frank M. White. *Viscous Fluid Flow*. McGraw-Hill, 2 edition, 1991.

[15] Peiqing Liu. Boundary Layer Theory and Its Approximation. In *Aerodynamics*, pages 307–393. Springer Nature Singapore, Singapore, 2022.

[16] Hamed Shahmohamadi and Mohammad Mehdi Rashidi. Experimental investigation and a novel analytical solution of turbulent boundary layer flow over a flat plate in a wind tunnel. *International Journal of Mechanical Sciences*, 133:121–128, 2017.

[17] Apollo. Aerodynamics Project Content. Technical report.

[18] Krüss-Scientific. Roughness (surface roughness). Technical report.

[19] D W F Brilman and M A Van Der Hoef. *TRANSPORT PHENOMENA Lecture notes FLUID DYNAMICS HEAT & MASS TRANSFER.*

[20] NIST. *NIST Chemistry WebBook, SRD 69.* 2023.

[21] J.E. Shingley and C.R. Mischke. Mechanical Engineering Design - Chapter 10: Mechanical Springs. chapter 10. McGraw-Hill, 8 edition, 1976.

[22] RK Rose. Profile technology. Technical report.

[23] Robert D. Blevins. *Flow induced Vibration.* Krieger Publishing Company, 2 edition, 2001.

[24] Ferdinand Beer, Jr. Johnsten, E. Russell, John DeWolf, and David Mazurek. *Mechanics of Materials.* McGraw-Hill Education, 6 edition, 2011.

[25] D.B. Martens. *Design of low stiffness flexures used for direct friction drag measurements of a tyre sidewall in the wind tunnel.* PhD thesis, University of Twente, Enschede, 2024.

[26] Novatech. F329 Deci-Newton Loadcell Standard Range 0.1N (10gf) Low force high resolution loadcell Best resolution 4 microNewton Passive Wheatstone bridge Foil strain gauges High thermal stability Durable design Translational deflection Specification. Technical report.

[27] Interface. Interface - Mini Load Cells.

[28] Sisco. Sisco - 0-5 N Digital Force Gauge, 0.001N. Technical report.

[29] Test Calibration Ametek Sensors. Chatillon Force Gauges.

[30] LTC. Minebea Co. ds-mm-cb17. Technical report.

[31] Trotec. Technische informatie-8086 Speedy 400 Lasergraveersysteem. Technical report.

[32] David R. H. Jones and Michael F. Ashby. *Engineering Materials 1 - An Introduction to Properties, Applications and Design.* Elsevier Science, 5 edition, 2019.

[33] Tim A. Osswald, Erwin Baur, and Natalie Rudolph. *Plastics Handbook: The Resource for Plastics Engineers.*

[34] ASM International. Aluminum and Aluminum Alloys.

[35] Sophocles J. Orfanidis. *Introduction to Signal Processing Second Edition.* Rutgers University, 2023.

[36] Jonathan W. Naughton. Surface Shear Stress Measurements. In *Optical Metrology for Fluids, Combustion and Solids*, pages 323–349. Springer US, Boston, MA, 2003.

[37] H H Bruun. Hot-Wire Anemometry: Principles and Signal Analysis. *Measurement Science and Technology*, 7(10), 10 1996.

[38] V. C. Patel. Calibration of the Preston tube and limitations on its use in pressure gradients. *Journal of Fluid Mechanics*, 23(01):185, 9 1965.

A Appendix

During the preparation of this work the author(s) used:

- ChatGPT in order to look for certain more formal synonyms and help with finding sources.
- Grammarly to help with structure and synonyms.

After using this tool/service, the author(s) reviewed and edited the content as needed and take(s) full responsibility for the content of the work.

A.1 List of Materials

Product	Material	Quantity and Dimensions
Wooden quarters gap-sealing ring	Plywood	4x: 900x400x6mm
Acrylic quarters gap-sealing ring	Acryl	4x: 900x400x5mm
Insert small tires	Acryl	1x: 450x500x10mm
Insert middle tires	Acryl	1x: 500x500x10mm
Insert big tires	Acryl	1x: 750x550x10mm
Outsert small tires	Acryl	1x: 900x600x10mm
Outsert middle tires	Acryl	1x: 900x600x10mm
Outsert big tires and flat plate	Acryl	2x: 800x450x10mm
Spacers gap-sealing ring	Aluminium	44x: 20x20x1mm
Leaf springs	Stainless steel	4x: 140x50x0.5mm
Wooden leaf spring reinforcement	Plywood	8x: 100x80x4mm
Elastic sealing band	Elastic Rubber	8825mm
Moving table	Blocan (Aluminum)	3x: 720x40x40mm
		2x: 1400x40x40mm
Clamping piece	Polycarbonate	1x: 650x1000x1000mm
Threaded center rod	Stainless steel	1x: 1500x10x10mm

Table A.1: List of materials used

A.2 Load cell data

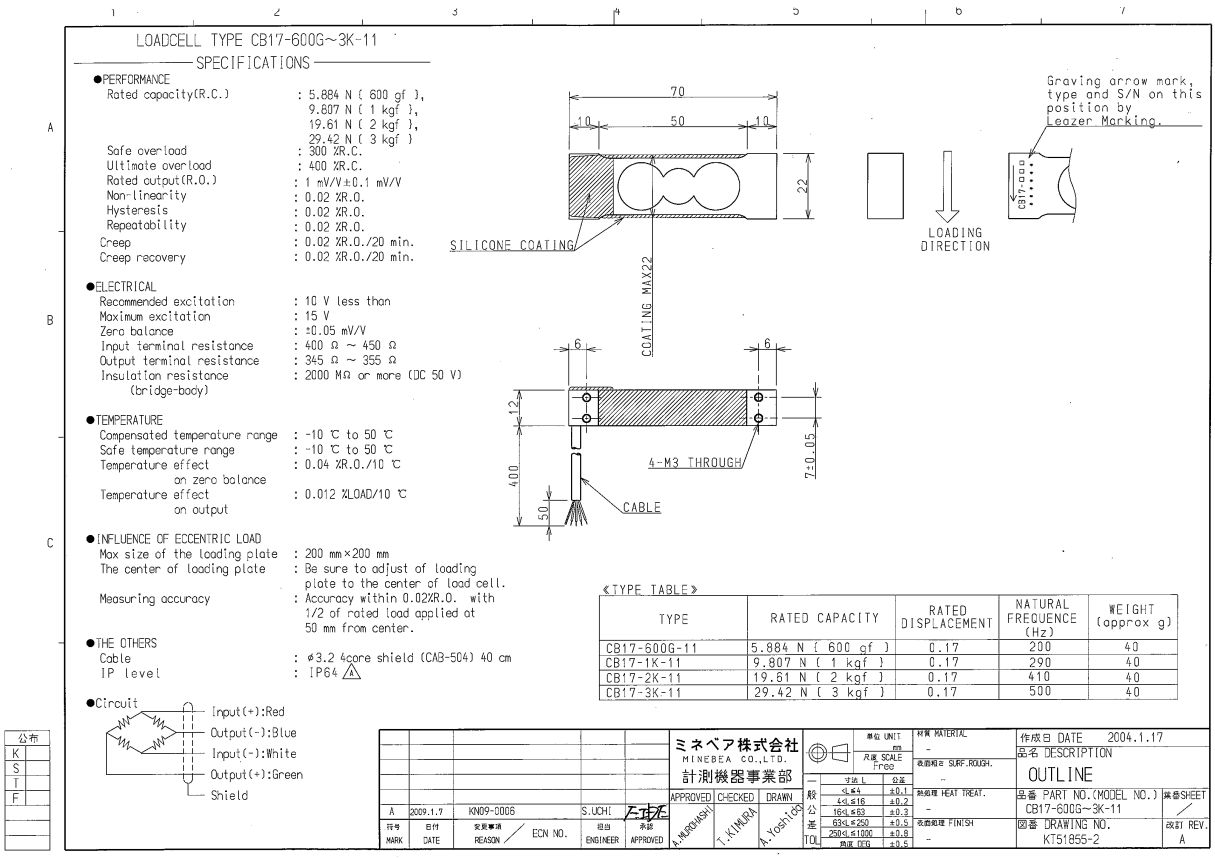

A.3 Real set-up

This section of the appendix presents the actual components used in the setup during testing.

Figure A.1: Side view of the wind tunnel

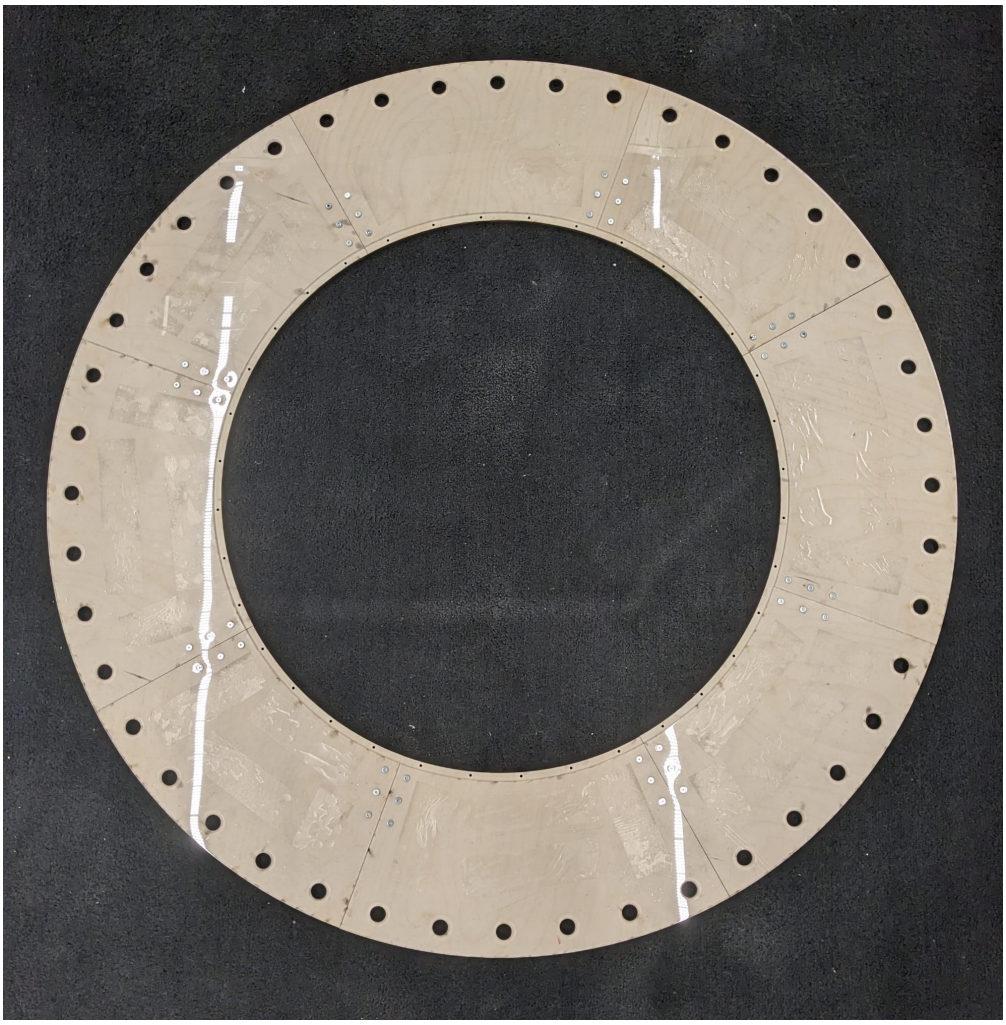

Figure A.2: Gap-sealing ring used in setup

Figure A.3: Mechanism to keep tire positioned in middle

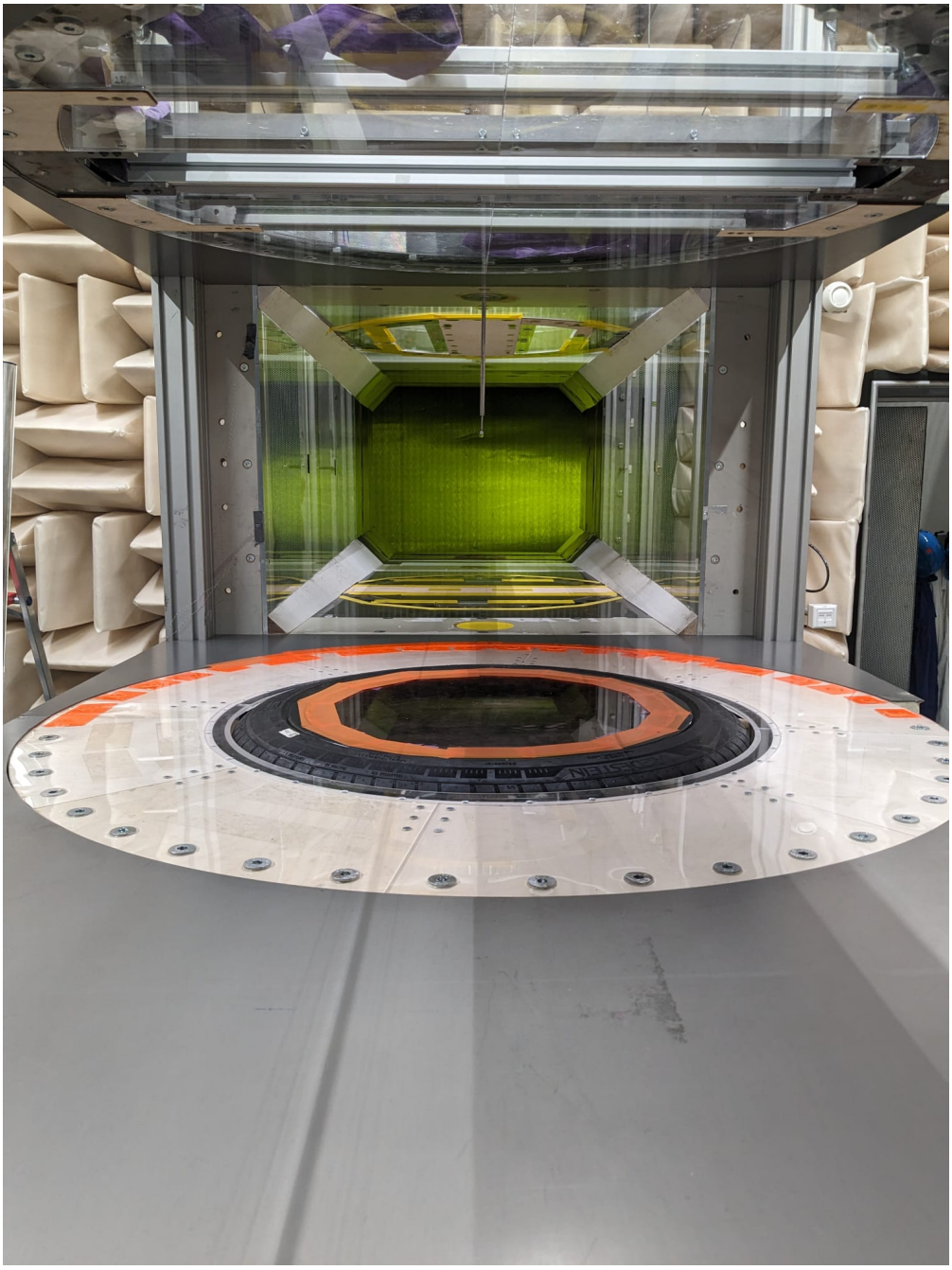

Figure A.4: Complete set-up front view

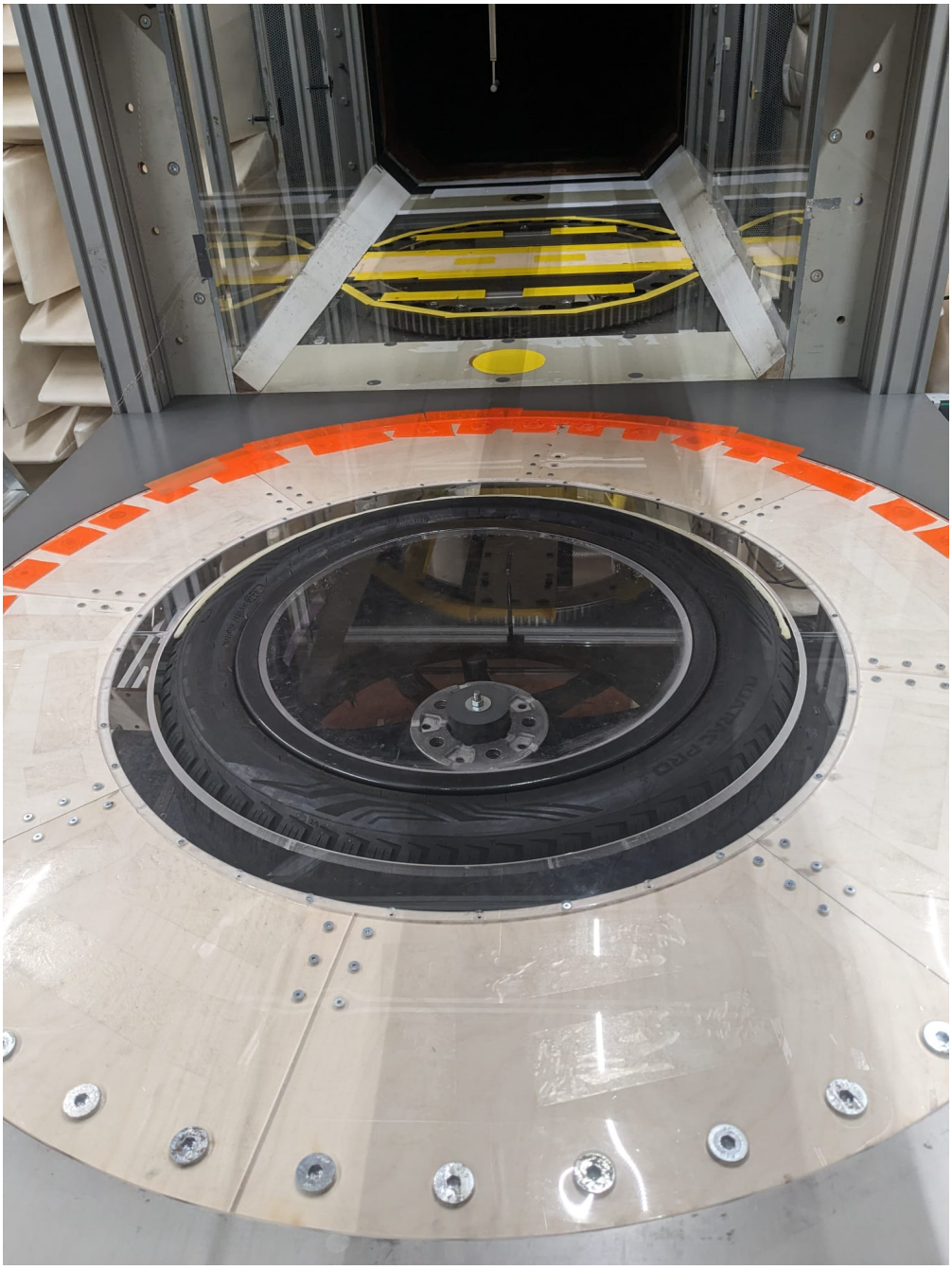

Figure A.5: Complete set-up top view

Figure A.6: Complete set-up bottom view

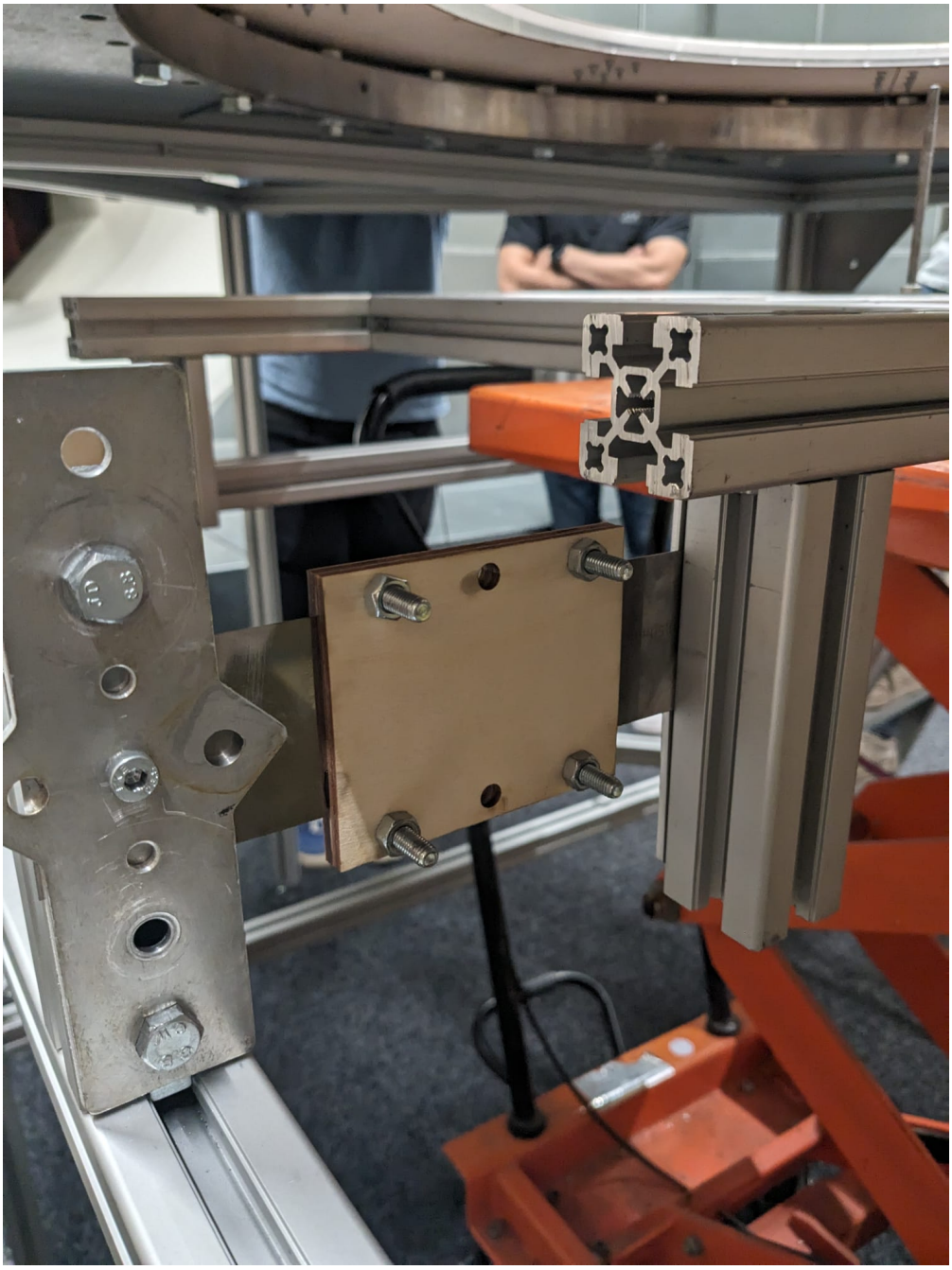

Figure A.7: Leaf springs used in setup

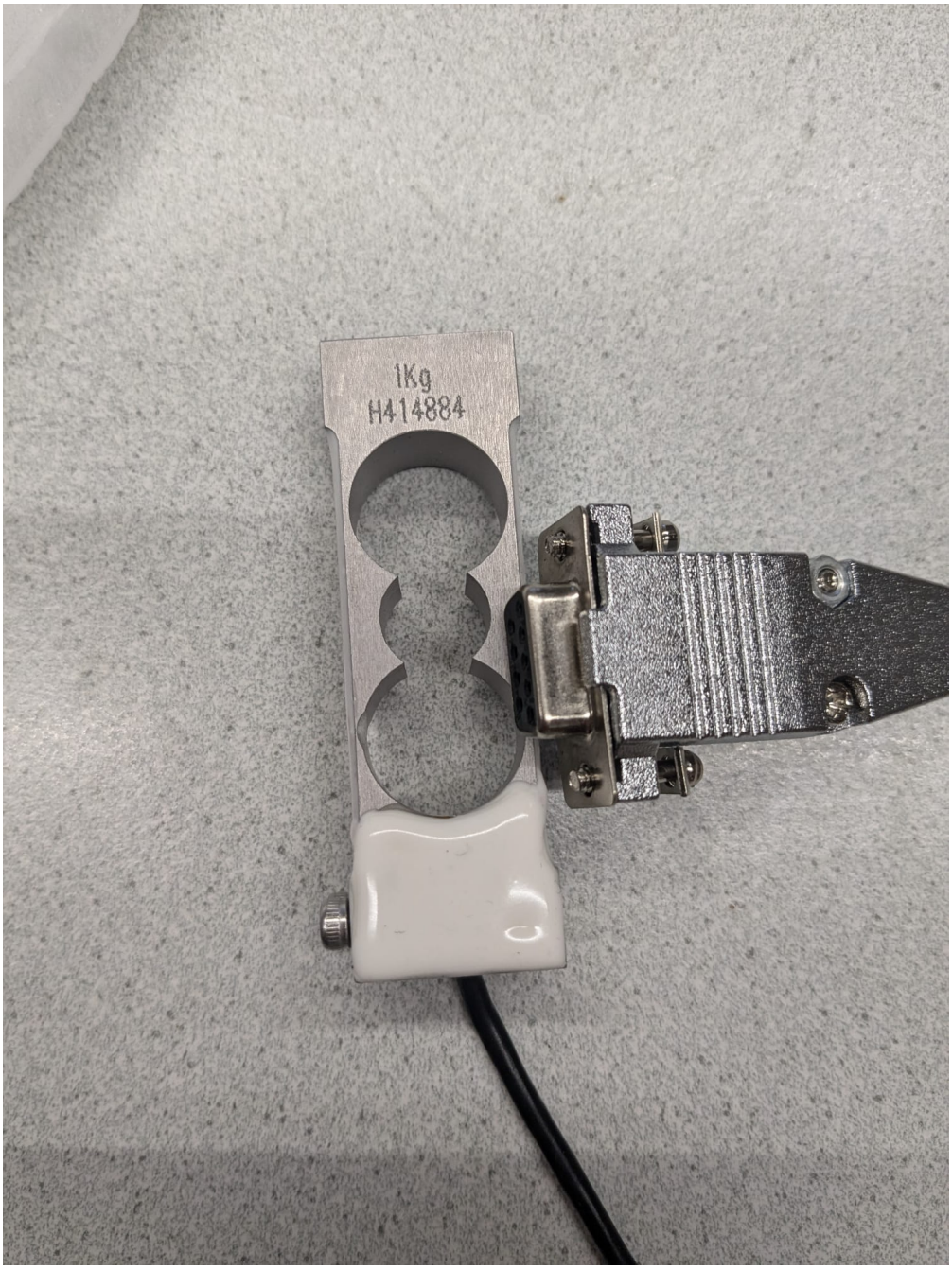

Figure A.8: Load cell used in setup